GENERAL PHYSICS

I. MOLECULAR BEAMS*

Academic and Research Staff

Prof. J. R. Zacharias
Prof. J. G. King
Prof. H. H. Brown
Dr. T. R. Brown
Dr. G. A. Herzlinger
Dr. E. H. Jacobsen
Dr. M. G. R. Thomson
Dr. J. C. Weaver
F. J. O'Brien

Graduate Students

S. A. Cohen
W. B. Davis
H. F. Dylla
J. A. Jarrell
D. G. Lysy
D. G. Payan
B. R. Silver
D. M. Payne
N. D. Punsky

RESEARCH OBJECTIVES AND SUMMARY OF RESEARCH

1. Molecular Microscopy

There are, in a broad sense, three kinds of microscopy characterized by the particles which carry information concerning the sample to the observer. Photons and charged particles have been extensively used in well-known ways, but the possibility of obtaining information from neutral molecules emitted by a sample in vacuum has apparently not been exploited to any significant degree. The idea of building a microscope that uses neutral molecules to obtain an image arose naturally from our studies of evaporation from liquid helium, but the molecular microscope, although useful in many fields of science and engineering, seems likely to prove most important in biological applications. This is because molecules carrying information from the sample interact through the same weak forces that are significant in biological interactions, and because the interactions are highly surface-specific (in contrast to photons and electrons which penetrate many atomic layers).

The object of our work in microscopy is (i) to study surface variations of weak forces (sites) by desorbing previously adsorbed neutral molecules by means of a technique that we call neutral molecule surface staining; (ii) to develop a new form of microprobe that is likely to be competitive with the ion and x-ray devices already in existence; and (iii) to study emissions of vapor and gas from biological samples. These emissions may occur spontaneously or as a result of electrical, chemical, or radiation stimuli.

There are many forms that this instrumentation can take, depending on the problem to be studied. Different provisions can be made for dead or live samples. Frog skin has been kept alive in one apparatus, and water emissions observed; the diffusion of water through tooth enamel has also been observed. The instrument can be built to have spatial resolution of varying degrees, temporal resolution, or mass resolution (i.e., the identification of emerging molecules by ionizing them and identifying them mass spectrometrically). The neutral emissions from the sample may occur simply as a result of the temperature of the sample, or after heating small areas with beams of charged particles or light, in which case the resolution can be that associated with the stimulating beam. A considerable pressure of water vapor in the apparatus is permissible, as long as excessive scattering does not take place. This tolerance may make possible the study of delicate biological samples with simultaneous spatial, temporal, and mass resolution, without excessive denaturing by dehydration.

In order to carry out this work, we are setting up cooperative programs with various

*This work was supported by the Joint Services Electronics Programs (U.S. Army, U.S. Navy, and U.S. Air Force) under Contract DAAB07-71-C-0300.

scientists in the Boston area. Our collaborators include Dr. S. Caplan (Harvard Medical School), A. Essig (New England Medical Center), and P. Robbins and D. Waugh (Department of Biology, M. I. T.).

2. Low-Temperature Atomic Beam Studies

Most of the low-temperature atomic beam studies that have been the focus of our interest in the last five years have been completed, and publications have been, or are being, prepared. Preliminary results have been obtained in two experiments: one in which pulses of heat stimulate evaporation in liquid helium, and another in which the dynamics of surface coverage by fractional monolayers on various substrates are studied by our techniques. We cannot afford the manpower and the expense of continuing this research, even though it has just reached the point of being well-developed technically and is of great interest. It seems likely that it will be taken up elsewhere. From our point of view, the fact that it has led to the development of molecular microscopy will perhaps have been its greatest value.

3. Electron Microscopy

The high-resolution high-contrast electron microscopy project that involves the development of new kinds of electron lenses using foils continues. Computation have been extended, and experimental studies have begun, of possible lens configurations, and of radiation damage that might prove troublesome as one attempts high resolution.

J. G. King

A. IN SITU MEASUREMENT OF VAPOR PRESSURE ABOVE SUBMONOLAYER HELIUM FILMS ON AN ARGON-COATED SUBSTRATE

1. Introduction

In recent years, research on helium submonolayers has proceeded rapidly, in part because of the simplicity of the helium substrate system. In principle, precise numerical calculations[1] based on various theoretical models can be compared with experimental data. Also, the study of helium is made more attractive by its characteristically weak interactions, low temperatures, small atomic mass, and isotopic effects. These indicate the possibility of cooperative quantum, as well as classical, phenomena.

Until recently, adsorption isotherms[2] and specific-heat[3] experiments were the source of measurements of the properties of submonolayer helium films. In 1970, however, Wallace and Goodstein[4] published data on adsorption isosteres, that is, measurements of pressure vs temperature at constant film coverage. Their data allowed immediate calculation of the isosteric heat of adsorption, Q_{ST}, and the differential molar entropy, $(\partial S/\partial n)_\theta$, two quantities that previously were obtained through indirect and imprecise convolution of isotherm data. Without knowing of their results, we undertook measurements of adsorption isosteres using different experimental techniques.

Preliminary results are reported to show the workability and advantages of our technique.

2. Theory

The pressure-temperature-coverage relation of an adsorbed layer in equilibrium with its gas phase can be derived from statistical mechanics. The relation is dependent on a model of the adatoms on the surface. The two most contrary models are complete localization (Langmuir) and complete mobility (Hill).[5] The P-T relationships are the following.

Localized

$$P = \frac{(2\pi m)^{3/2}}{h^3} (kT)^{5/2} \frac{1}{j_n} \exp(-Q/T) \frac{\theta}{1-\theta} \exp(\theta z V/kT),$$

where

Z = number of nearest neighbors

V = energy of interaction between nearest neighbors

M = mass of adatom

Q = energy of adsorption of single atom in the limit of $\theta \to 0$, $T \to 0°K$

θ = fraction of a monolayer.

Mobile

$$P = \frac{(2\pi m)^{1/2}}{hb} (kT)^{3/2} \frac{1}{j_n} \exp(-Q/T) \frac{\theta}{1-\theta} \exp\left(\frac{\theta}{1-\theta} - \frac{2a\theta}{bkT}\right),$$

where j_n = partition function for the vibration of an adsorbed atom perpendicular to the surface.

The adsorbed atoms obey a two-dimensional van der Waals equation

$$\left(\phi + a\frac{N^2}{A^2}\right)(A-Nb) = NkT.$$

In the limit of low temperatures, the exponential term dominates the relation, and the power of the temperature is not discernible. Thus we cannot immediately use pressure-temperature data to choose the correct model. Yet the isosteric heat of adsorption and the differential molar entropy can still be obtained. The heat of adsorption can be used to determine the interaction of adatoms with each other, the a/b and ZV terms in the two different equations. These two-dimensional van der Waals

constants can then be compared with three-dimensional ones.[6] The differential molar entropy can be integrated to yield the total absolute entropy, which can be compared with specific-heat data.

The differential molar entropy, $(\partial S/\partial n)_\theta$, is given by

$$\left(\frac{\partial S}{\partial n}\right)_\theta = -RT \ln P + S_G,$$

where $S_G = 3/2\ R \ln T$ is the entropy of the gas phase. We assume that T varies so slightly that its power-law dependence is excluded from consideration, as in our data where T varies from 1.3°K to 2.1°K and Q_{ST} is approximately 70°K/atom.

3. Apparatus and Procedures

The apparatus is a 5-liter brass can containing an Allen-type electron multiplier and a field-ionization needle. The can is evacuated to $P = 1 \times 10^{-7}$ Torr and slowly cooled to 77°K. Enough argon is admitted to cover the macroscopic internal area of the can and its contents with 5 layers of atoms. The argon is allowed to equilibrate at 77°K for 10 hours. Adsorption isotherms under similar conditions by previous researchers[7] show the formation of a complete monolayer of argon. Next the can is cooled in 1 hour to a temperature of 4.2°K, and a calibrated amount of He^4 is then admitted to the can. The amount is approximately enough to cover 1/2 of the macroscopic area with helium atoms. (The density of a completed monolayer, as determined by other researchers,[8] is 7.8×10^{14} atoms/cm^2.) The field ionizer, which faces the first dynode of the multiplier, is raised to +10 kV. Helium atoms in the gas phase that come within ~1000 Å of the tip are ionized, and accelerated to the first dynode. Electron multiplication takes place. The pulses are amplified and counted by using standard pulse-counting techniques. The count rate (C. R.) is recorded at various temperatures. It is related to the pressure by the formula: $\text{C. R.} = K \dfrac{P\ (\text{Torr})}{\sqrt{T}\,(°\text{K})}$, where K is approximately $2 \times 10^{+12}$ $(°\text{K})^{1/2}$/Torr sec. (Previous experiments[9] have shown that the sensitivity of the needle is not greater for slow atoms than fast ones.)

Because the pressure at most is 10^{-6} Torr at 4°K with monolayer coverage, the number of atoms in the gas phase is 1.3×10^{16} atoms, while the number of adsorbed atoms is approximately 2×10^{18}. Consequently, as the can cools down, the areal density of atoms on the surface changes little, and thus the process is isosteric.

The data are plotted in the form ln (C. R.) $T^{1/2}$ vs 1/T, the slope of which is Q_{ST}. The differential molar entropy is the slope of ln ($T^{1/2}$C. R.) vs ln T. The slopes are determined by a least-squares fit. The error in the slope is determined by repeating the runs and using an eyeball fit to set upper and lower limits on the slopes

of the numerous runs.

Equilibration times between temperature changes are of the order of 15 min, which is 5 times as long as necessary for restabilizing the helium bath temperature within a millidegree (below the λ-point) by using a servo-controlled pumping line and heater. This time allows the unadsorbed helium atoms in excess of 10^6 collisions with the walls to thermalize. Calculations show that the brass can is within 10^{-3} °K of bath temperature after 10 seconds. Measurement of the temperatures of the electron multiplier and field-ionization detector show that they do not get colder than 10°K. They are isolated from the bath and do not follow its variations over the time scale of data taking.

4. Results

Data for 3 runs at the same coverage are plotted in Figs. I-1 and I-2. Figure I-1 shows the isosteric heat; Fig. I-2 shows the differential molar entropy; and Fig. I-3 shows

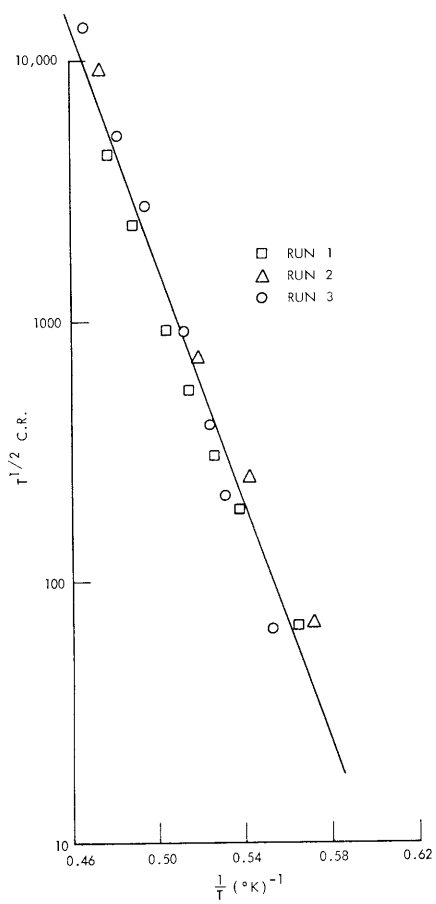

Fig. I-1.

Three runs taken with ~1 monolayer coverage in the apparatus. Slope = Q_{ST} = 61.5 ± .8°K/atom.

the isosteric heat of adsorption Q_{ST} and differential molar entropy of He^4 on argon-coated brass. Three runs were taken at each of 3 different coverages. The absolute

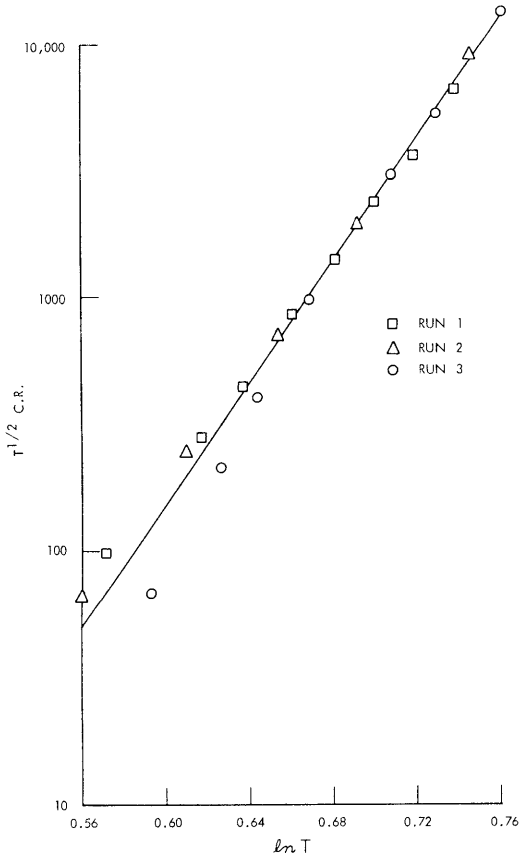

Fig. I-2.

Three runs taken with ~1 monolayer coverage in the apparatus. Slope = $\frac{(\partial S/\partial n)_\theta - S_G}{R}$ = 28.1 ± 4.1.

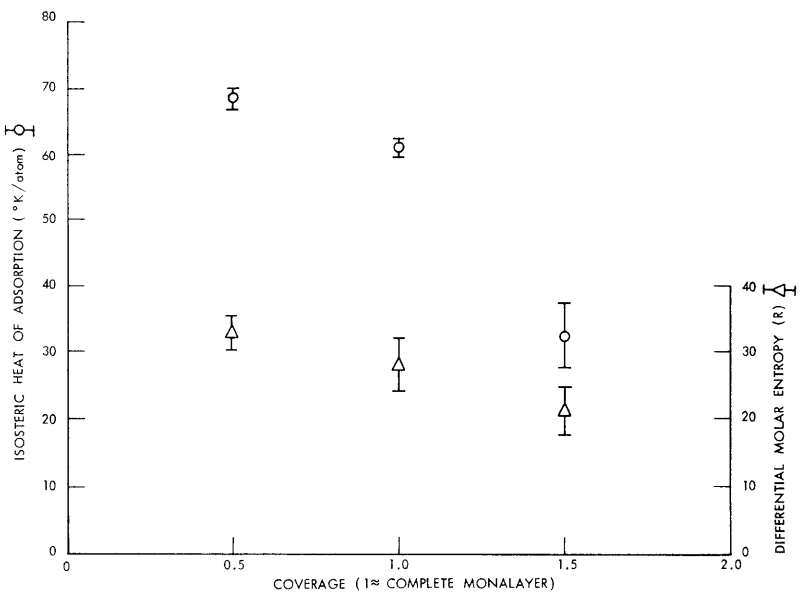

Fig. I-3. Isosteric heat of adsorption, Q_{ST}, and differential molar entropy, R, of He^4 on argon-coated brass, taken with 3 different coverages. The absolute coverage is unknown, but it is estimated that a complete monolayer equals 1.

coverage has not been determined because of the small surface area of the can. Comparison of these data (under the assumption of a microscopic surface area equal to the macroscopic area) with those of Wallace and Goodstein (see Fig. I-4) who used a copper sponge

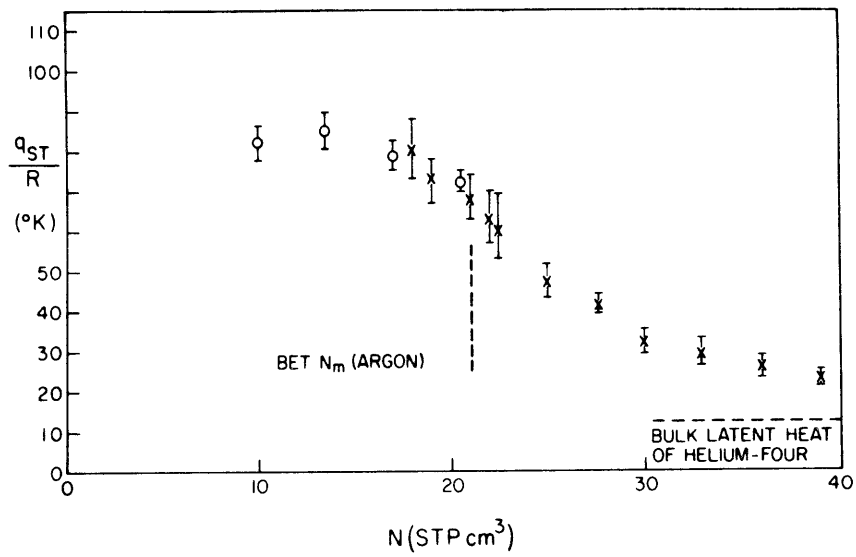

Fig. I-4. Isosteric heat of adsorption vs coverage in the first two layers of He^4 adsorbed on one layer of argon. High coverage data marked by X. [From Fig. 5 in Wallace and Goodstein,[4] reproduced with the permission of the Journal of Low Temperature Physics.]

coated with argon as a substrate and an ion gauge as a detector, shows the similarity in shape and absolute value. Wallace and Goodstein find heats of adsorption at $\theta = 1/2$ for He on other noble-gas-coated copper sponges to be in the same range, 70°K/atom to 110°K/atom. The major reason for comparing our data with Wallace and Goodstein's is to emphasize the workability of our method. Also, the field-ionization detector can function in the pressure range 10^{-6} to 10^{-13} Torr, thereby extending data to much lower coverages, pressures, and temperatures. These measurements are performed in situ; hence, uncertainties in the Weber-Schmidt equation, caused by conditions of the surface of the tube connecting the pressure sensor to the apparatus, are eliminated. Thus the previously inaccessible region of ultralow coverage is available for experiments with adsorption isosteres and isotherms.

S. A. Cohen

References

1. See, for example, A. Novaco and F. Milford, J. Low Temp. Phys. 3, 307 (1970).

2. See, for example, J. P. Hobson, Can. J. Phys. 37, 300 (1959).
3. J. Dash and G. Stewart, Phys. Rev. A 2, 918 (1970).
4. J. L. Wallace and D. L. Goodstein, J. Low Temp. Phys. 3, 283 (1970).
5. See, for example, R. H. Fowler, Statistical Mechanics (Cambridge University Press, London, 1956).
6. J. H. de Boer, The Dynamical Character of Adsorption (Clarendon Press, Oxford, 1968).
7. D. M. Young and A. D. Crowell, Physical Adsorption of Gases (Butterworths Scientific Publications, London, 1962).
8. M. Ross and W. Steele, J. Chem. Phys. 35, 862 (1961).
9. W. D. Johnston, Ph. D. Thesis, Department of Physics, M. I. T., February 1966 (unpublished).

B. MEASUREMENT OF He^3-He^3 AND He^4-He^4 CROSS SECTIONS AT LOW TEMPERATURES

1. Introduction

We have performed atomic-beam scattering experiments on He^3 and He^4 isotopes in the temperature range 1.5°K to 2.1°K, extending the work of D. E. Oates.[1] The data on He^4-He^4 yield a total cross section of 128 ± 17 $\mathring{A}^2$ in agreement with that previously reported by Oates and King.[1] The He^3-He^3 total cross section is 87.7 ± 9 $\mathring{A}^2$. The velocity-dependent cross sections of both have also been obtained.

2. Apparatus and Procedures

The novel components of the apparatus have been described previously.[2] The principal features are common to many atomic-beam attenuation experiments. A helium beam is sent through a chopper and then through a gas-filled scattering chamber. The arrival of helium atoms that have passed through the scattering chamber is detected by a field ionizer and recorded by a multichannel scaler as a function of time. Comparison of beam intensities for runs with the scattering chamber full and empty yield the scattering cross section.

Calculated cross sections comply with those defined by Berkling et al.[3] We use the basic attenuation formula for a velocity-analyzed beam of intensity $I_o(v)$ passing through a scattering chamber of length L filled with gas at a temperature, T, and number density, n,

$$I(v) = I_o(v) \exp[-L\, n\, Q_{eff}(v, T)].$$

$Q_{eff}(v, T)$ is related to the actual cross section Q(g) derived from partial wave analysis applied to a particular interatomic potential by

$$Q_{eff}(v, T) = \iiint Q(g) \frac{\bar{g}}{\bar{v}} \frac{1}{\pi^{3/2}} \frac{1}{\alpha^3} \exp\left(-v_k^2/\alpha^2\right) \sin\theta_k \, d\theta_k d\phi_k d\bar{v}_k,$$

where subscript k refers to the scattering gas $\bar{g} = \bar{v} - \bar{v}_k$, and $\alpha = \sqrt{\frac{2k_B T}{m}}$. The total cross section, $\bar{Q}_{eff}$, is given by

$$\bar{Q}_{eff} = \int Q_{eff}(v, T) f(v) \, dv,$$

where f(v) is the velocity distribution in the beam.

3. He^4-He^4 Results

Runs were made at 2.11°K and 1.75°K. The data at 2.11°K yield a total cross section, $\bar{Q}_{eff}$, of 128 ± 17 $\mathring{A}^2$, in agreement with that reported earlier,[1] 144 ± 16 $\mathring{A}^2$. The 13% error in the data is calculated on a basis of statistics (8%) and estimated systematic errors. The velocity-dependent cross section data at 2.11°K is presented in Fig. I-5, together with the earlier data of Oates. The error bars are calculated from the actual scatter in the data. The uncertainty in velocity resolution, because of finite widths of the aperture function and multichannel analyzer time bins, is indicated at three characteristic velocities. The structure previously reported by Oates[1] at v = 127 m/s appears in the new data at 133 m/s, just within the velocity resolution. Experiments were performed to check for possible equipment error. In particular, the multichannel scaler was allowed to accumulate 500,000 background counts with all equipment running. The channels in which the peak occurred were within 1/2 of standard deviation of the average. Thus, to the best of our knowledge, there was no instrumental error.

To resolve the problem, additional data were taken at 1.75°K. We expected that if a scattering resonance were present it would manifest itself more clearly in the lower temperature data. Because resonances occur at specific values of angular momentum and energy, it was expected that a resonance at lower T would be at a greater beam velocity $\left(\frac{\Delta v}{v} = \frac{1}{2} \frac{\Delta T}{T}\right)$ to compensate for the lower scattering gas velocities. The data at 1.75°K are plotted in Fig. I-6. There is no peak at 130 ± 9 m/s.

4. He^3-He^3 Results

He^3 runs were performed at 1.55°K so that the velocity distribution would be the same as in the He^4 runs at 2.1°K. The total cross section was found to be 87.7 ± 9 $\mathring{A}^2$. The velocity-dependent cross section is shown in Fig. I-7. The ratio

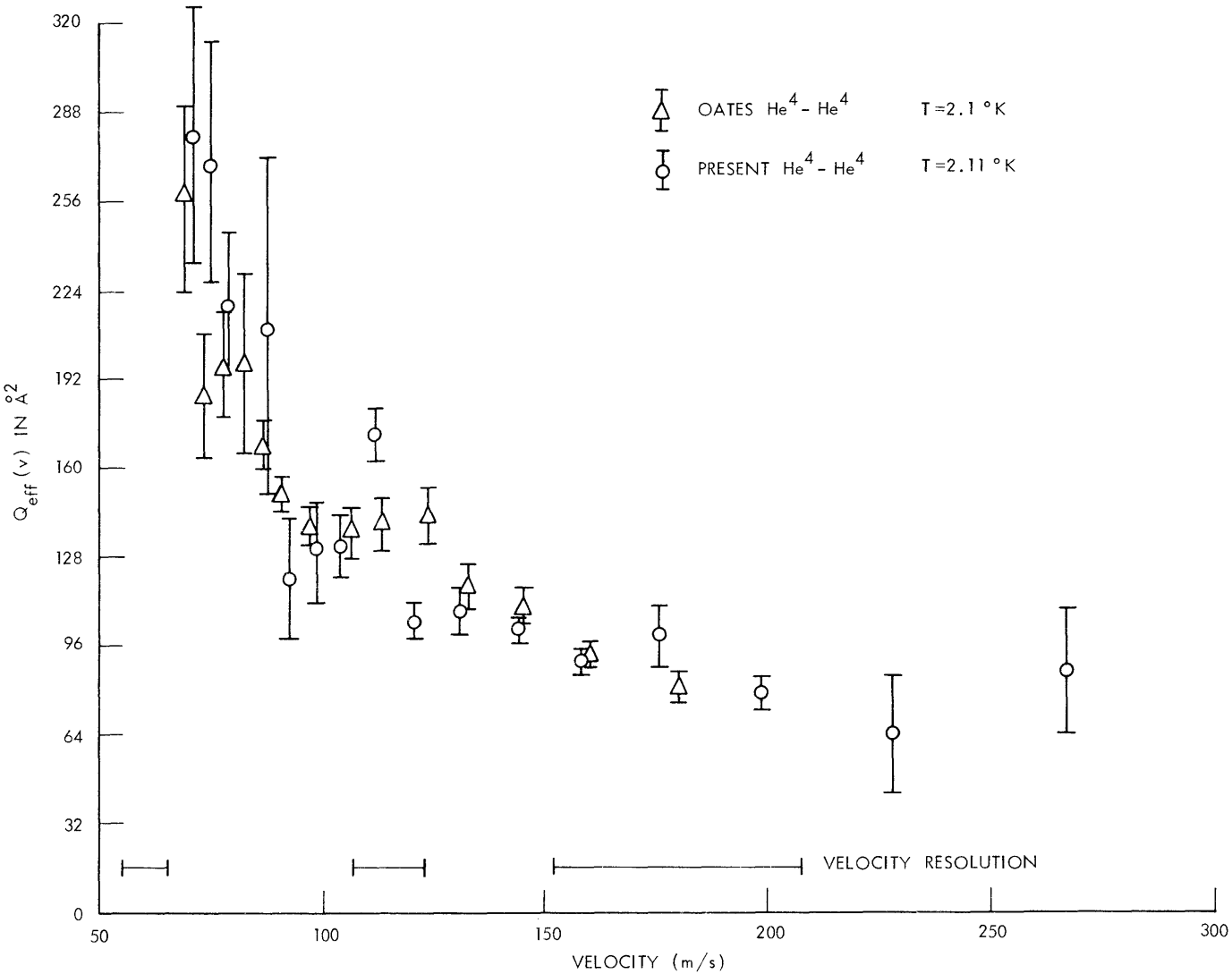

Fig. I-5. He^4-He^4 scattering: velocity-dependent cross section, $Q_{eff}(v)$, vs beam velocity. Scattering gas temperature is 2.11°K.

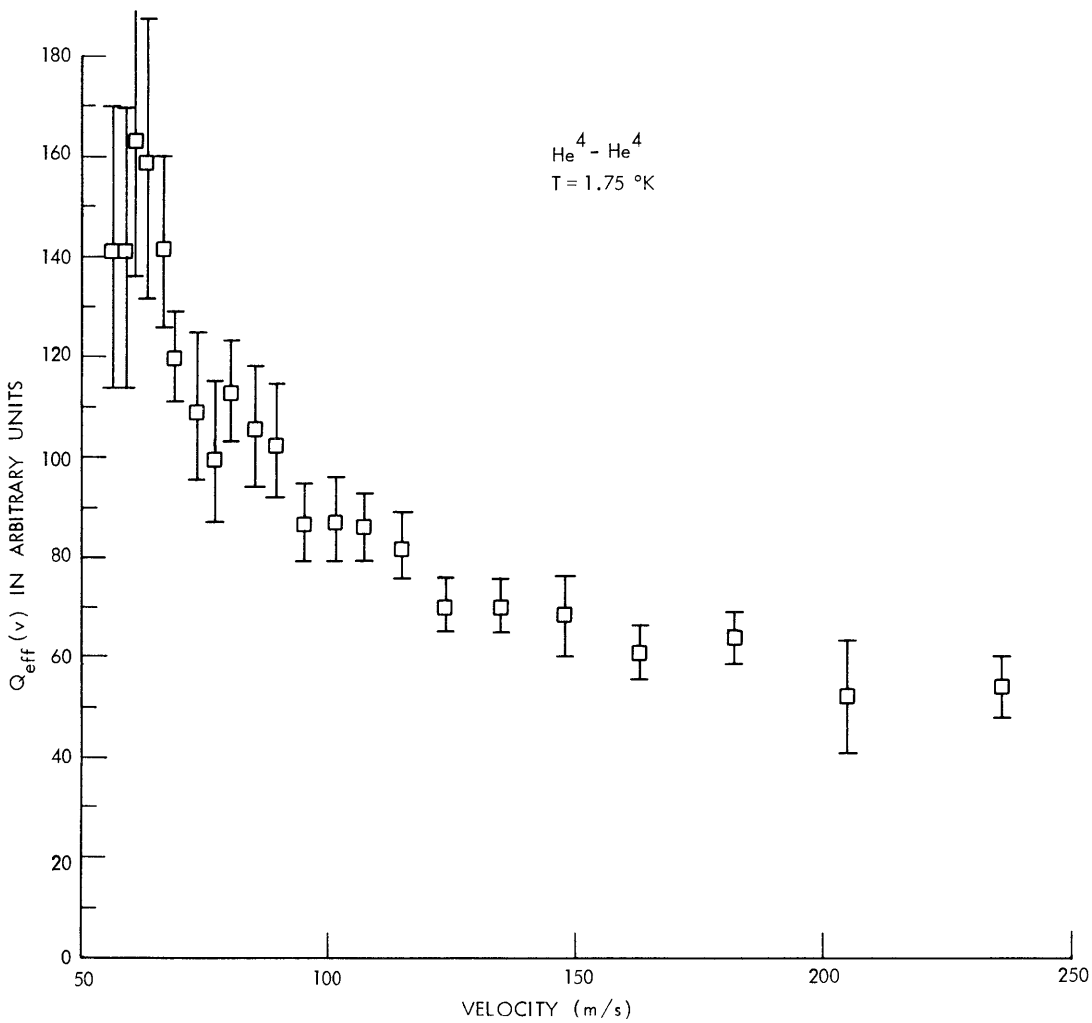

Fig. I-6. He^4-He^4 scattering: velocity-dependent cross section, $Q_{eff}(v)$, vs beam velocity. Scattering gas temperature is 1.75°K.

of the He^3-He^3 total cross section to the He^4-He^4 total cross section (the average of old and new data) is 0.65 ± .09. This cannot be directly compared with other transport-phenomena data such as viscosity, because of the different weighting given to velocity intervals in the calculation of their cross sections.

Each different theoretical interaction potential yields a different ratio of He^3 to He^4 cross sections. We have calculated this ratio for a Lennard-Jones potential with $r_m = 2.56$ Å and $\epsilon = 1.4 \times 10^{-15}$ erg. This yielded 0.48 ± .07. (The large error results from the graphical manner in which $\overline{Q}_{eff}$ was calculated.) We did not expect that this would fit the data as the velocity-dependent cross section calculated with the L-J potential fails to fit the shape and absolute value of the He^4-He^4

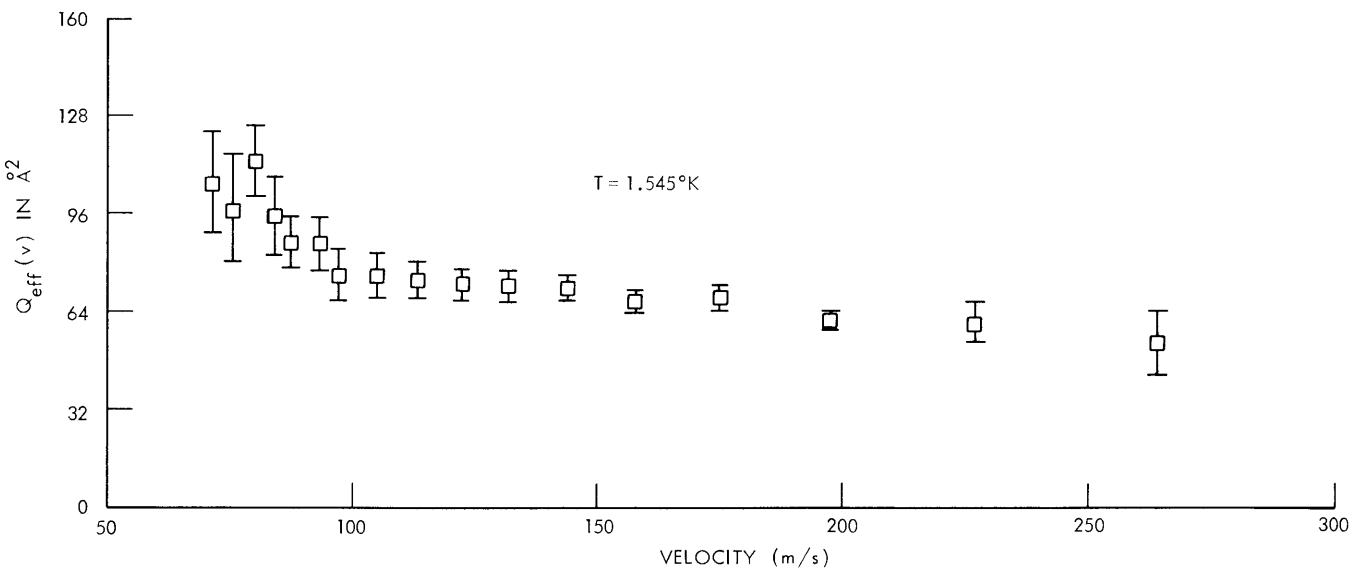

Fig. I-7. He^3-He^3 scattering: velocity-dependent cross section, $Q_{eff}(v)$, vs beam velocity. Scattering gas temperature is 1.55°K.

cross sections.[1] Calculations are planned for other potentials.

The difference in cross section displayed by He^3 and He^4, which provides direct evidence of the different quantum statistics obeyed by the two isotopes, may provide as sensitive a method for choosing the correct interaction potential as fitting the velocity-dependent cross section.

This report was written while D. E. Oates was at Universität Bonn. The data were taken and reduced over a period of 3 months using apparatus that Oates had constructed and perfected in 3 years.

S. A. Cohen, D. E. Oates, J. G. King

References

1. D. E. Oates and J. G. King, Phys. Rev. Letters 26, 735 (1971).
2. D. E. Oates, Quarterly Progress Report No. 98, Research Laboratory of Electronics, M.I.T., July 15, 1970, pp. 1-4.
3. K. Berkling, R. Helbing, K. Kramer, H. Pauly, Ch. Schlier, and P. Toschek, "Effektive Stobquerschnitte bei Streuversuchen," Z. Physik 166, 406 (1962).

C. INVESTIGATION OF MOBILITY OF SUBMONOLAYER HELIUM FILMS BY ATOMIC-BEAM TECHNIQUES

1. Introduction

Research on helium submonolayer films has followed classical methods: study of adsorption isotherms,[1] adsorption isosteres,[2] and specific heat.[3] These methods yield a direct measure of the various heats of adsorption, the monolayer density vs pressure, and the temperature and coverage dependences of the specific heat and the entropy. These quantities can be compared with numerical calculations based on models of the state of the adsorbed atoms. The most realistic models are two-dimensional analogs of three-dimensional systems, including van der Waals gas, ideal or condensed Bose (or Fermi) gases, Einstein solid, or Debye solid with tunneling bonds. The quantity most commonly used to show the distinction among the gas, liquid, and solid states – the mobility of adatoms – has not, however, been directly observed.

In this report we describe an experiment using atomic-beam techniques by which the mobility of helium adatoms on an argon substrate near 2°K can be measured. Preliminary data, indicating no measurable mobility, are reported. We also report additional information on characteristic desorption times and velocities derived from the data.

2. Theoretical Predictions

Mobility of adatoms on a periodic surface could be caused by thermal hopping or quantum-mechanical tunneling between adjacent potential minima. An early calculation

by Hill[4] predicted that thermal hopping should be negligible at temperatures below $E_1/10k$, where E_1 is the depth of the well. The heat of adsorption is measured[2] to be ~70°K/atom at coverages less than a monolayer. That calculated by Ricca et al.[5] and by Novaco and Milford[6] is close to 100°K/atom, but varies up to 200°K if the argon lattice changes from a 100 to a 111 face. This poor agreement is not unexpected, since the experimental helium lattice is probably neither 100 or 111. Nevertheless, Ricca et al. give a reasonable estimate of E as 100°K. Therefore thermal hopping will probably not occur in the temperature region investigated in this experiment.

Calculations on quantum-mechanical tunneling by Ricca et al.,[5] J. Dash,[7] McCormick et al.,[8] Novaco and Milford,[6] and H. W. Lai et al.[9] predict tunneling for helium adsorbed on various noble-gas substrates. It must be stressed that the lattice parameters critically affect the tunneling time. Ricca reports rapid tunneling on the 111 face of argon, but none on the 100 face. Lai et al. report different calculations with similar results. Dash and his co-workers, using a third calculation technique, also show the importance of small changes in lattice dimensions. Typical tunneling times predicted by these researchers vary from 10^{-10} to 10^{-12} s.

3. Experiment

The method used to measure the mobility of the helium atoms on a preadsorbed argon substrate at 2.0°K is as follows. First, approximately a monolayer of helium is adsorbed on a large argon-coated surface. A small area of the surface, ~1 mm^2, is then rapidly heated to ~30°K. This desorbs the helium atoms, which are detected, and their arrival times are recorded. That small area is then rapidly cooled back to 2°K. If the helium adatoms are mobile, some from adjacent areas will soon diffuse over the 1-mm^2 area. This area can be reheated at a later time and the number of desorbed atoms can be compared with the original number.

The major components of the apparatus are a brass vacuum chamber containing an Al_2O_3 wafer, a field-ionization detector and an electron multiplier. (See Fig. I-8.) The Al_2O_3 wafer is the heart of the experiment. Its construction is detailed in Fig. I-9. A pressed Al_2O_3 "superstrate," 1 × 1 × .027 in., with an average grain size of ~5000 Å, was obtained from the MRC Corporation. A strip of No. 302 stainless-steel foil, 1 in. × 1 cm × 2.50×10^{-4} cm, was epoxied across its center. The epoxy film, TRACON 2115, covered the stainless-steel foil with a thickness of $(1.5 \pm 1) \times 10^{-4}$ cm, as measured by optical interference techniques. Two strips, 1 mm wide, 2000 Å thick, one of Pb, the other of In, were evaporated over the epoxy, perpendicular to the stainless-steel foil, near one end. Four-point electrical connections were made to the evaporated strips; two connections were made to the No. 302 stainless-steel foil. The contacts were made of pressed In. The back of the wafer was coated with a light film of Apiezon N grease to achieve better thermal contact to an O. F. H. C. copper

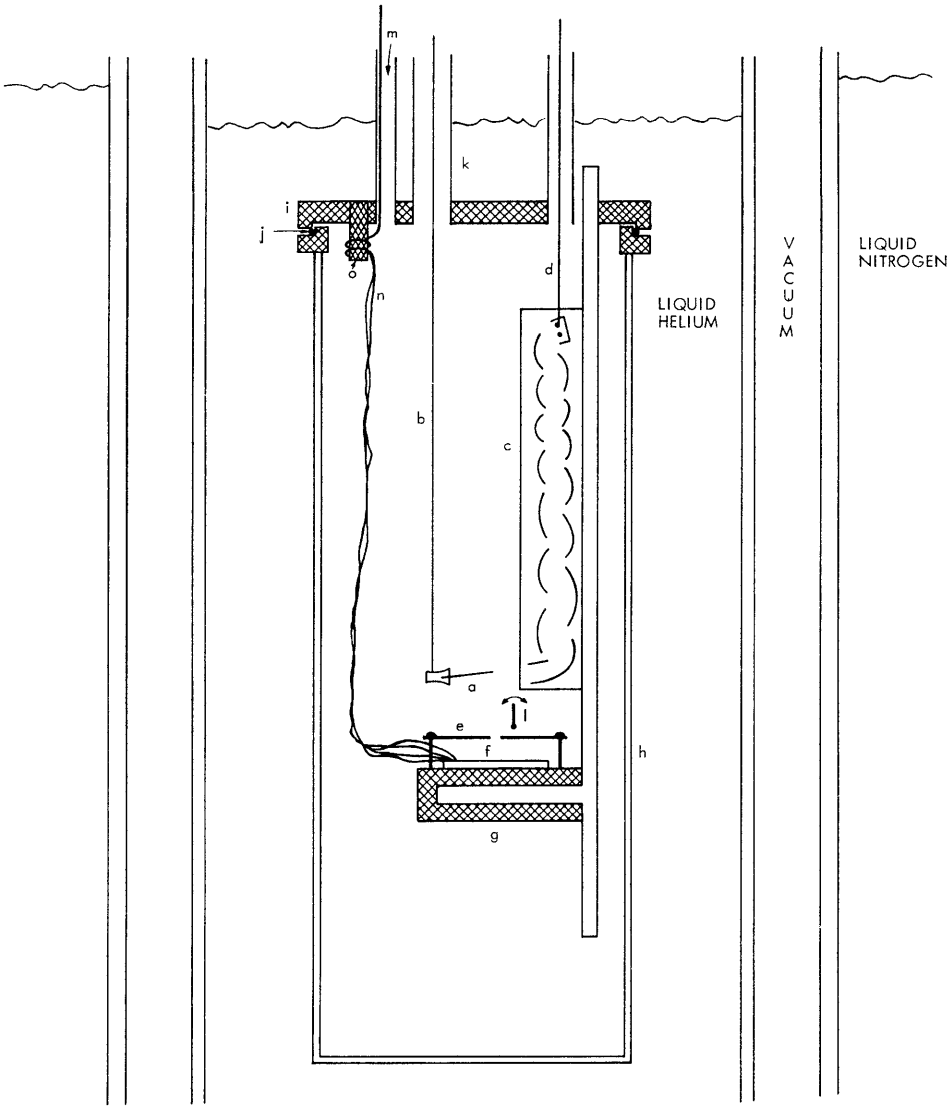

(a) FIELD IONIZATION NEEDLE
(b) COPPER WIRE CONNECTING NEEDLE TO 10 kV POWER SUPPLY
(c) ELECTRON MULTIPLIER
(d) SIGNAL LEAD
(e) PINHOLE
(f) Al_2O_3 WAFER
(g) HOLLOW OFHC COPPER BLOCK FILLED WITH LIQUID HELIUM
(h) BRASS CAN
(i) STAINLESS-STEEL FLANGE
(j) LEAD INDIUM O-RING SEAL
(k) TUBE TO DIFFUSION PUMP
(l) MOVABLE SHUTTER
(m) GAS INLET TUBE
(n) LEADS TO Al_2O_3 WAFER
(o) HEAT SINK FOR LEADS

Fig. I-8. Apparatus for studying mobility of submonolayer helium films.

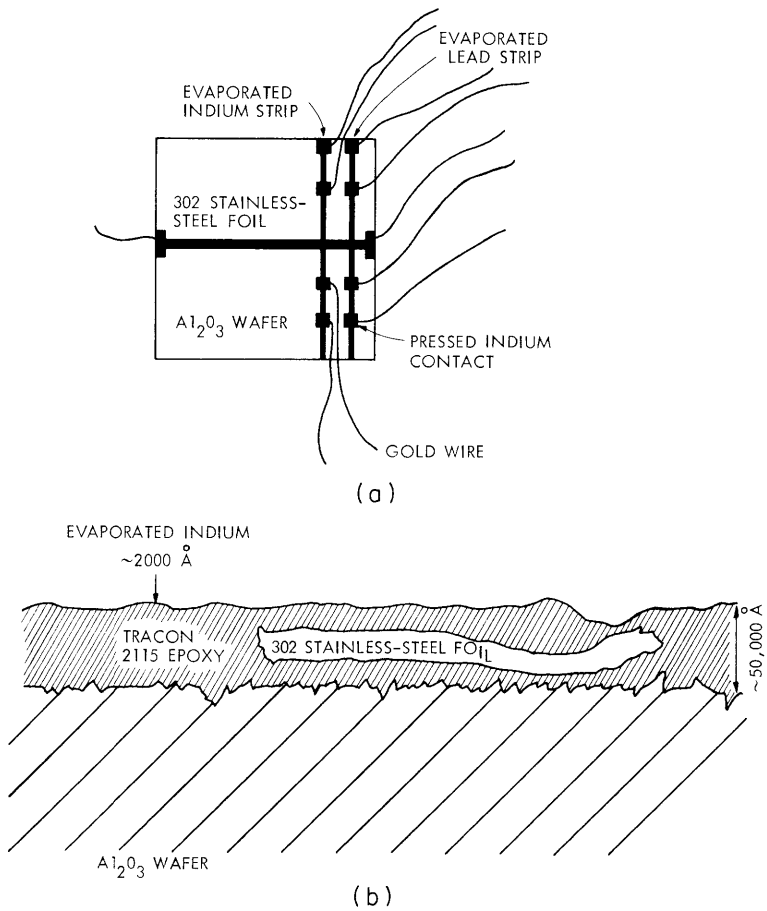

Fig. I-9. Details of the construction of Al_2O_3 substrate. (Not to scale.) (a) Top view. (b) Cross section.

block. The wafer was placed on the block, a 1-mm pinhole collimator was placed 5 mm above the wafer and the field ionizer, and a tungsten needle with a tip of 1000 Å diameter was placed 2 cm above the pinhole, facing the first dynode of the electron multiplier. The brass can containing this assembly was sealed, evacuated to $P = 1 \times 10^{-7}$ Torr and slowly cooled to 77°K. Enough argon was admitted to coat the macroscopic inner area of the can and its contents with 5 monolayers of argon. Previous experiments[8] have shown that argon forms a complete monolayer at this temperature. Equilibration was allowed for 10 hours at 77°K. The can was then cooled to 4.2°K by liquid helium. In our experiment, the copper block is directly connected to the helium bath by a stainless-steel capillary, thereby ensuring thermal contact. The field ionizer is raised to +10 kV. Any helium atom that comes within ~1000 Å of the tip is ionized and accelerated to the electron multiplier. Normal pulse-counting techniques with 0.5 μs resolution are used to record the pulses. Simple kinetic theory predicts a counting rate, C.R.,

equal to 2×10^{12} P(Torr)/$\sqrt{T}$ (°K), where K is approximately 2×10^{12} (°K)$^{1/2}$/Torr sec. The pressure above a submonolayer film of helium is typically 10^{-12} Torr. Thus the background counting rate at 2.0°K is ~100 count/sec. A current pulse of 1-μs width and 3-A magnitude, containing enough energy to heat a thermally isolated foil from 2°K to 30°K can be supplied to the foil by an SCR. The temperature of the foil can be known at two points – the superconducting transitions of the In and Pb films, 3.4°K and 7.2°K, respectively. The IV characteristics of these films can be monitored by a differential amplifier with a 1-μs response time. Thus the experiment has the following steps: heating the stainless-steel foil; detecting the temperature rise; detecting the desorbed atoms that pass through the pinhole and come within 1000 Å of the field-ionization tip; recording the time of arrival of the atoms (on a storage oscilloscope); observing the cooling down of the foil; waiting for helium atoms on the unheated portions of the Al_2O_3 wafer to diffuse over the central portion; and repeating the process.

It is important to note the characteristic times and numbers associated with the experiment.

a. Time to recover the central portion by adatom mobility. If the tunneling time is 10^{-12} s and the separation of adsorption sites is 3 Å, then, by random walk, it takes ~10^{13} steps to move 1 mm. This implies a recovery time of ~10 s.

b. Time to recover the central portion by vapor deposition. If the background pressure is (at worst) 10^{-10} Torr, then the flux of atoms in the gas is 5×10^{11} atoms/cm^2 s. Since the density of a completed monolayer of helium is 8×10^{14} atoms/cm^2, it would take 1.6×10^3 s to recover the area.

c. Time to transfer sufficient energy to the helium atoms for desorption. The energy transfer to the foil is limited by the RC of the circuit. The present arrangement has RC = 0.5 μs, with a sufficient L to cause critical damping. Transfer of energy through the epoxy to the Al_2O_3 superstrate and to the argon and helium monolayers should take place in a characteristic time $t = \rho\ell^2\frac{c}{K}$, where ρ is the density of the epoxy, ℓ its thickness, c its specific heat near T = 20°K, and K its thermal conductivity at T = 20°K. Using typical values for insulators, we arrive at $t \approx 1$ μs. Thus as energy is being dumped into the foil it is probably being transferred to the Al_2O_3 wafer and the helium monolayer.

d. Time for the helium atoms to desorb once the substrate is raised to 20°K (adsorption isotherms show that there is virtually no adsorbed helium at 20°K). An estimate of this time using Kapitza resistance of thick, 1000 Å films in the limit of thin films, gives ~10^{-7} s. A calculation by Ying and Bendow,[10] using a 3-d multiphonon theory, gives $t = 2\times10^{-8}$ s for Ne on Xe-covered graphite. (It appears that we can measure this characteristic time if we eliminate the epoxy over the foil and use shorter heat pulses.)

e. Time for desorbed atoms to get to the detector. This is

$$t = \frac{s(2\text{ cm})}{V\text{ thermal}} \approx 10^{-4}\text{ s.}$$

f. Number of atoms detected if a full monolayer is desorbed. This is $n = n_o\Omega$, where Ω is the solid angle of the detector, and n_o is the number of atoms that get through the pinhole. Under these circumstances, $n \approx 50$. These last two characteristic times and numbers yield a counting rate during the 0.1 ms after heating of 5×10^5 counts/s, more than 1000 times the normal background.

g. Rise in background count rate from desorption of 1 mm × 1 in. area of a helium monolayer. Simple kinetic theory yields 10^4 counts/s.

h. Decay time of the background count rate. This time depends on the probability of adsorption. (Because the characteristic distance that helium atoms not going through the pinhole must travel is ~20 cm, this background will arrive long after the initial burst of atoms.) Monitoring the decay of this background will yield a good estimate of the probability of sticking.

4. Results

A run was made with an Al_2O_3 substrate different from the one described above. It lacked the temperature-measuring superconducting In and Pb films. It also lacked an epoxy layer over the stainless-steel foil. The epoxy under the foil was approximately 5×10^{-3} cm thick. This changed the theoretical cooling-off time to ~1 ms. The copper block was not well connected to the bath; its temperature never fell below 3.1°K, as measured by a resistance thermometer mounted on the block. Also, the detector was 5 cm from the foil.

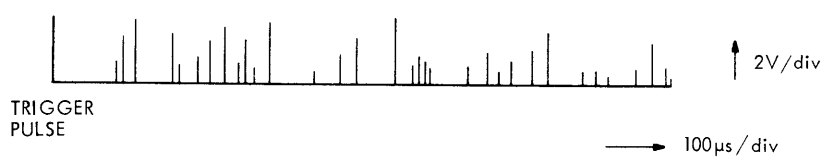

Fig. I-10. Oscilloscope trace of output from atom detection system following first heat pulse. Pulsewidths are ~0.5 μs. Distribution in pulse heights results from characteristics of the electron multiplier.

Helium gas was admitted and the procedure outlined above was followed. After admission of the helium, the count rate rose to 1.3×10^4 counts/s. It fell slowly to ~1000 counts/s. A pulse of current sufficient to raise the foil to 35°K was sent through

the foil. The signal, as recorded from the storage oscilloscope is shown in Fig. I-10. Thirty-one atoms were detected in the 1 ms immediately following the heat pulse. The foil was pulsed once each minute for the next 11 min. A total of 9 counts was accumulated, in agreement with background. The foil was then pulse-heated at time intervals of 8, 16, and 24 min.

The 8-min pulses showed approximately 4 counts per sweep. The 16-min and 24-min pulses showed approximately 17 counts/sweep. (A sweep is the 1 ms following the heat pulse.) Increasing the heat pulse to raise the temperature to 50°K did not increase the number of counts. Not enough data were taken for a detailed statistical analysis of velocity distribution, or counts vs delay time. The major point is evident, however. It took in excess of 10^3 s for a monolayer to reform. This is consistent with vapor deposition, not mobility.

The major problem is the accurate determination of the temperature of the foil. We hope that the use of the In and Pb films will solve that problem. If, contrary to calculation, the foil does not cool down in 1 ms, it could drastically affect the situation.

More experiments are planned in which In and Pb films and better information-storage techniques will be used. Calculations and experiments are in progress that will determine the time-dependent temperature profile across the epoxy Al_2O_3 wafer. Experiments are planned to measure the desorption times and desorbed atom velocity distribution. Different substrates are also under consideration.

We are indebted to Professor Margaret L. A. MacVicar, of the Department of Physics, M. I. T., for suggesting the use of thin superconducting films as thermometers, and to J. G. King for suggesting the problem.

S. A. Cohen

References

1. See, for example, W. H. Keesom and J. Schweers, Physica 8, 1020-1043 (1941).
2. See, for example, J. Wallace and D. Goodstein, J. Low Temp. Phys. 3, 283 (1970).
3. See, for example, G. Stewart and J. Dash, J. Low Temp. Phys. 5, 1 (1971).
4. T. Hill, J. Chem. Phys. 14, 441 (1946).
5. F. Ricca, C. Pisani, and E. Garrone, J. Chem. Phys. 51, 4079 (1969).
6. F. Milford and A. Novaco, Phys. Rev. A 4, 1136 (1971).
7. J. Dash, J. Chem. Phys. 48, 2820 (1968).
8. W. D. McCormick, D. L. Goodstein, and J. G. Dash, Phys. Rev. 168, 249 (1968).
9. H. Lai, C. Woo, and F. Wu, J. Low Temp. Phys. 3, 463 (1970).
10. S. Ying and B. Bendow, Phys. Letters 37A, 91 (1971).

D. EVAPORATION OF NEUTRAL ATOMS FROM He II STIMULATED BY HEAT PULSES

1. Introduction

In a previous report,[1] we described an apparatus built to study the evaporation of neutral atoms from He II stimulated by heat pulses. This report discusses preliminary results and gives some calculations that indicate a better experimental configuration to study heat pulses in He II.

2. Apparatus

Several modifications to the apparatus described in a previous report[1] will be discussed briefly. We were unable to fill the He^4 pot quickly, and a large heat leak resulted from film flow in the fill capillary. We therefore installed a new fill capillary that is not connected to the He^3 refrigerator system or to the He^4 pot (Fig. I-11). Gaseous helium is condensed in the fill tube in the He^4 bath and allowed to drop directly into the He^4 pot at bath temperature from the end of a 0.020 in. ID capillary. We are able to fill the 0.05 cm^3 He II pot in less than 5 min by this method without overloading the He^3 refrigerator.

When we first tried filling the He^4 pot, we found that the He^3 superheated and boiled suddenly because of the low thermal conductivity of liquid He^3. Therefore it was necessary to redesign the He^3 pot in order to improve the heat transfer into the He^3 and to prevent large thermal gradients in the liquid that decreased the efficiency of the refrigerator. We now use a large-volume pot and maximize the He^3 copper surface ratio by filling this volume with copper wire and sintered copper (Fig. I-12).

3. Electronics

Pulses are supplied to the heater in the He^4 pot by the following method (Fig. I-13). A master trigger pulse starts the sweep of the multichannel analyzer used in the scaling or counting mode. One hundred twenty-eight channels are used, each channel having a 62.5 μs time span of which 25 μs is dead time for memory cycling. The master trigger pulse also triggers a delay generator which in turn provides the trigger for the General Radio 1217-C pulser. The output of the pulser, variable in pulse height and width, is applied to the heater in the He^4. The voltage and current pulses to the heater, monitored by the oscilloscope, measure the total energy supplied to the heater during the pulse.

Atoms that have evaporated from the He^4 surface pass through a small aperture and are field-ionized at the tip of the sharp tungsten needle (Fig. I-11). The

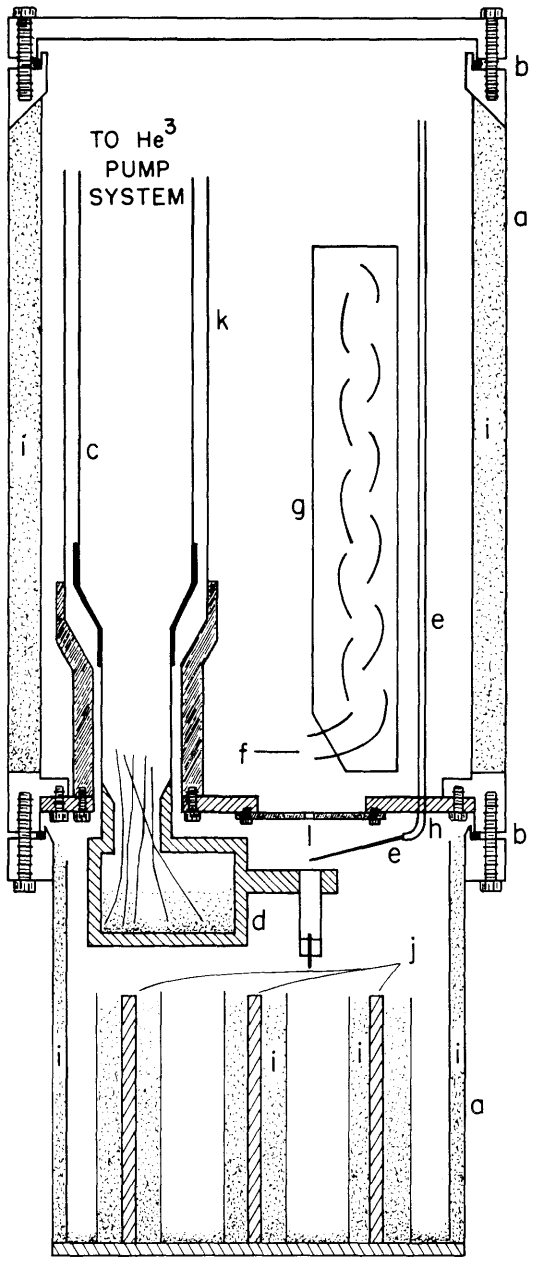

SOURCE CHAMBER ZEOLITE PUMP

(a) STAINLESS STEEL CHAMBER
(b) LEAD O-RING SEAL
(c) He^3 PUMP LINE
(d) He^3-He^4 POT STRUCTURE
(e) He^4 FILL LINE
(f) FIELD IONIZING NEEDLE
(g) ELECTRON MULTIPLIER
(h) COPPER SEPTUM
(i) ZEOLITE
(j) COPPER RODS AT BATH TEMPERATURE
(k) SOURCE CHAMBER ISOLATION LINE
(l) PINHOLE

Fig. I-11. Modified apparatus for studying the evaporation of helium atoms from He II stimulated by heat pulses.

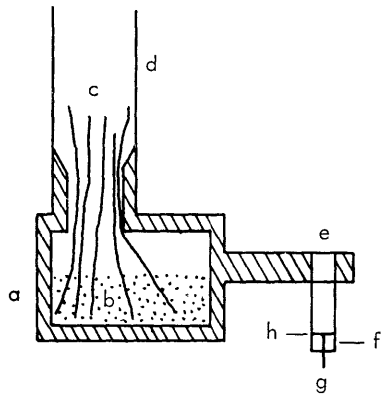

Fig. I-12. He^3-He^4 pot structure.

(a) He^3 POT
(b) SINTERED COPPER
(c) COPPER WIRE HEAT CONDUCTORS
(d) He^3 PUMP LINE
(e) He^4 POT
(f) EPOXY BOTTOM
(g) HEATER LEAD
(h) AQUADAG HEATER

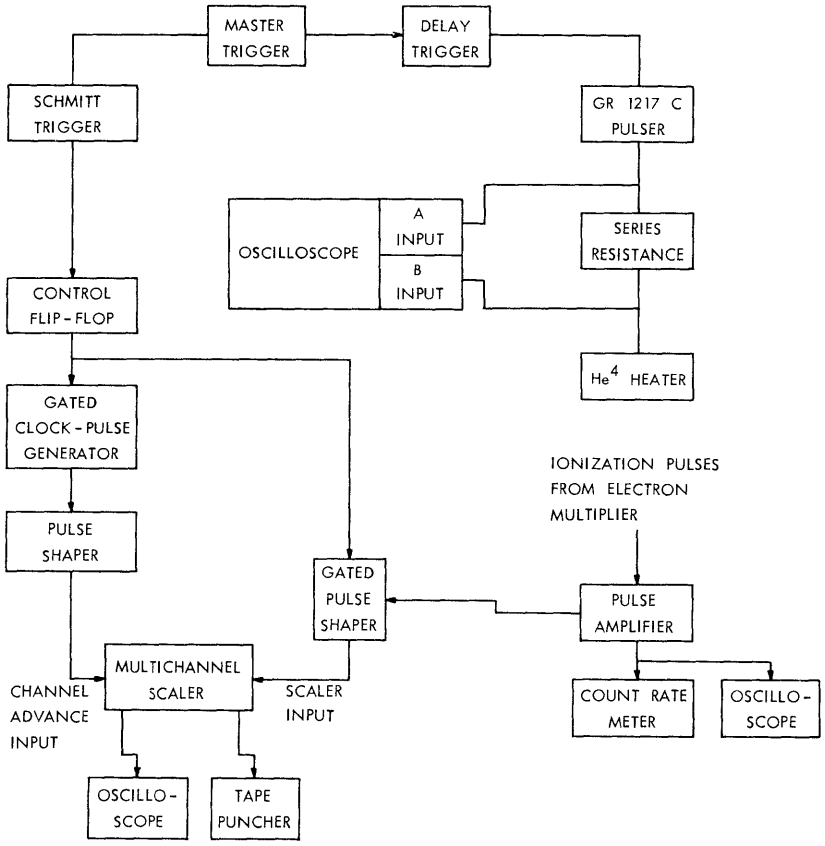

Fig. I-13. Experimental arrangement.

ions are collected on the front dynode of a 16-stage Allen-type electron multiplier, and the resultant pulses are amplified and then counted by the multichannel analyzer.

4. Preliminary Results

After a 16-hour cool-down period at 1.2°K, the background counting rate in the detection chamber is 1-2 counts/s, corresponding to pressures in the range 10^{-12}-10^{-13} Torr. A known volume of helium gas is admitted to the fill tube and after condensing in the bath at 1.2°K drops into the He^4 pot. The counting rate during filling rises to 6.5×10^5 counts/s and remains steady during 5-min fill time. After filling, the count rate falls off very rapidly and the temperature of the He^4 drops from 0.5°K (maintained during the fill) to 0.30°K.

Heat pulses, of 50-μs width, ranging from 0.01 to 40 erg per pulse are then put into the He^4. The counts due to the resultant evaporating atoms are stored in the

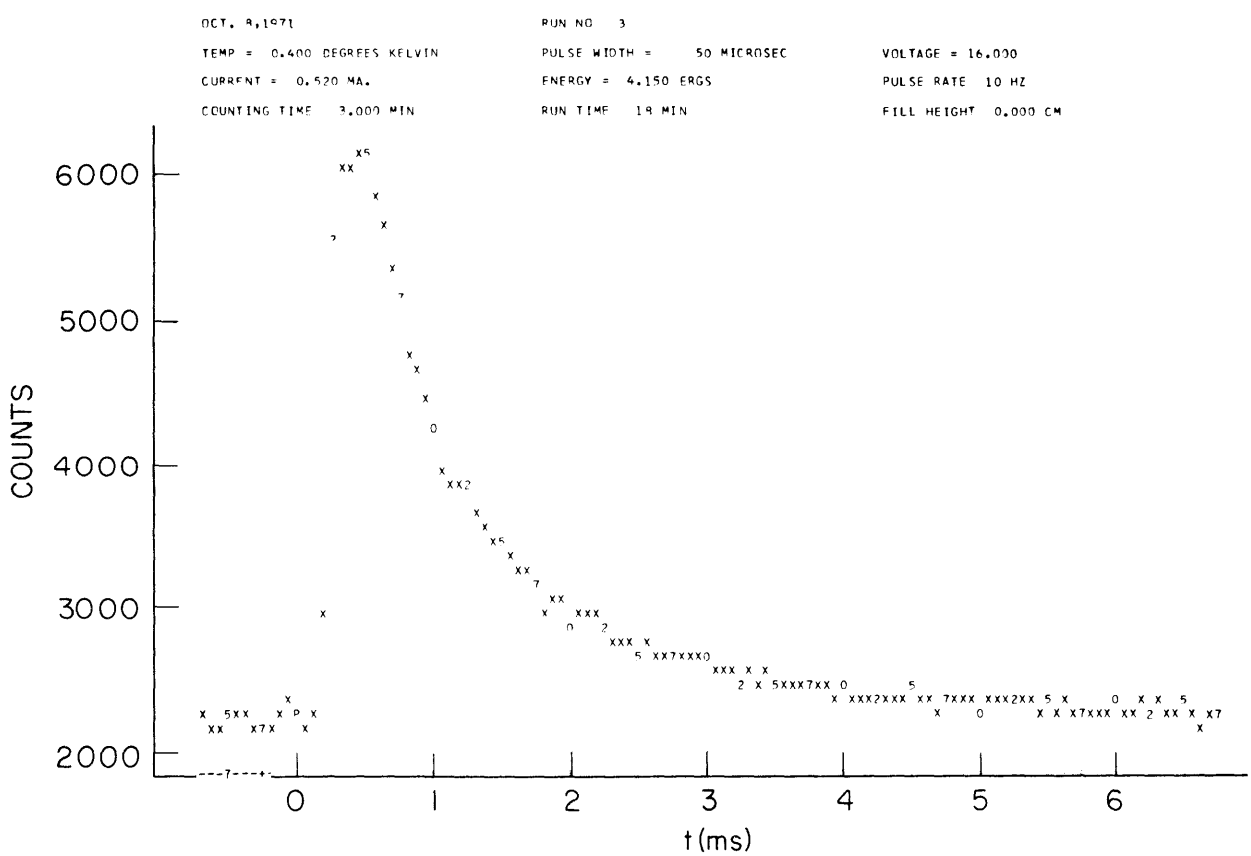

Fig. I-14. Multichannel analyzer output, showing distribution time of arrival of evaporating atoms.

multichannel analyzer, the output of which gives the arrival time distribution of the evaporating atoms at the needle. A typical multichannel output is shown in Fig. I-14.

From the multichannel output we are able to determine the number of counts/heat pulse by computing the area under the curve shown in Fig. I-13 and subtracting a background counting rate determined from channels 3-16 on the output. This number is plotted as a function of energy per heat pulse in Fig. I-15. From this figure we see

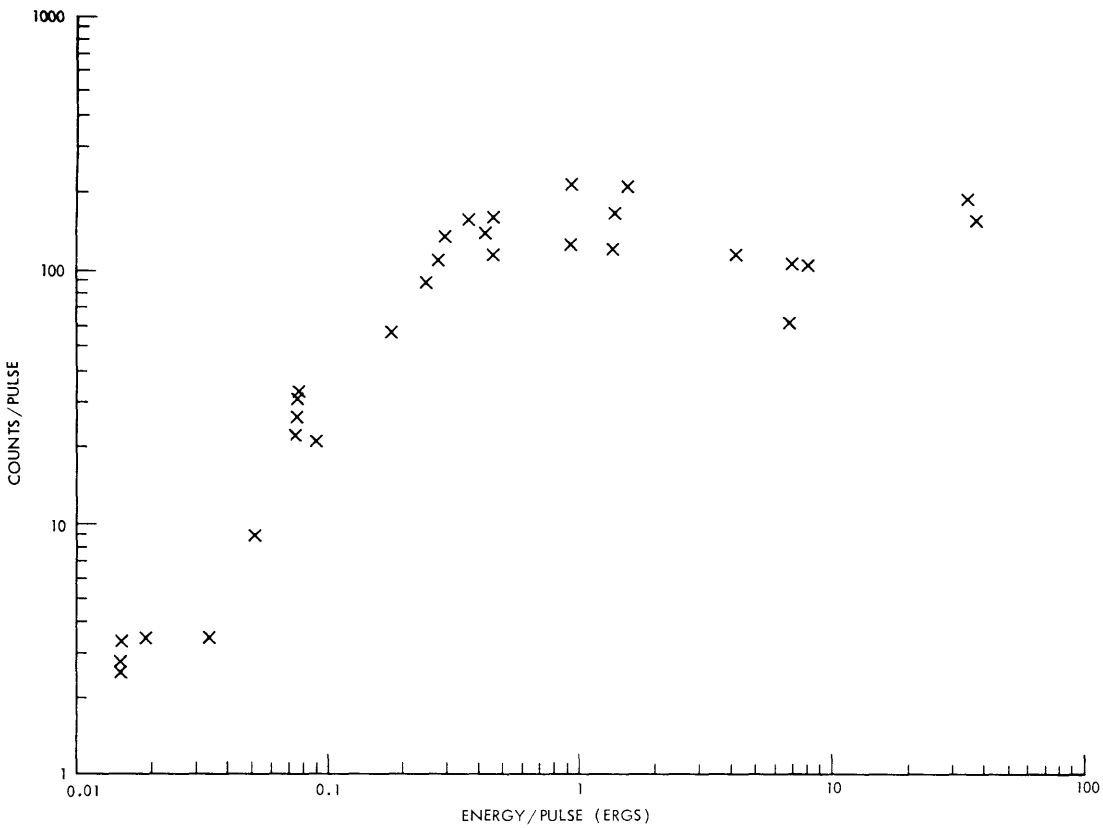

Fig. 1-15. Counts/pulse as a function of heat input/pulse.

that above ≈0.5 erg/pulse, the number of evaporating atoms/heat pulse remains approximately constant as we increase the energy/pulse. Under the assumption of a constant phonon-evaporating atom conversion ratio at the surface of the liquid He^4, this flattening of the curve could be due to a combination of Kapitza resistance at the carbon film-liquid helium interface and the creation of a gas film at the interface that then limits the heat flow across the boundary. We can get a rough measure of the surface temperature of the carbon film from a measurement of the resistance vs temperature curve for the heater. This measurement indicates that the surface of the heater warms up

considerably during the heat pulses, and for the higher energy pulses reaches 300°K.

If we plot the channel number of the first discernible rise of the heat pulse in the multichannel output vs energy of the heat pulse, we find that the arrival times for the beginning of the pulse decrease with increasing pulse energy (Fig. I-16).

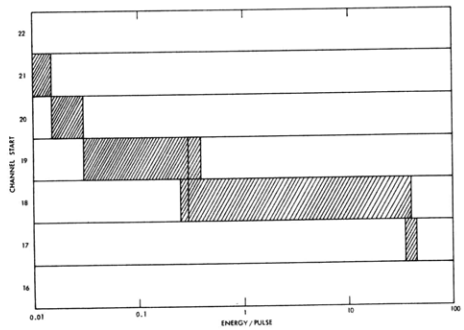

Fig. I-16. Start of pulse at the detector as a function of heat input/pulse.

In order to explain this effect, we must explore the processes by which a heat pulse is transformed into evaporating atoms. The heat pulse raises the surface temperature of the heater, which then can be thought of as a blackbody phonon radiator, characterized by an effective temperature T_H. The phonons radiated by the heater must be coupled into the liquid He II by a complex process that includes a thermal boundary resistance known as the Kapitza resistance. The phonons, coupled into the He II, have an unknown frequency distribution, but must all travel at the speed of sound (240 m/s), and make few collisions with each other or with the thermal phonons present at these temperatures, since the phonon mean-free path is long compared with the dimensions of the container. Those phonons in the solid angle that intercept the surface travel directly to the surface and arrive after a time ℓ/c, where ℓ is heater-to-surface distance. For a 1-cm distance this delay time is ~40 μs. Other phonons that are present scatter from the walls, diffusely and specularly, and arrive at the surface at times greater than ℓ/c. Those phonons that scatter from the walls and arrive at the surface only after many collisions with the walls form a diffusivelike flow of heat, the equation of which has been solved.[2]

At the interface, phonons are converted into evaporating atoms by a process that is still not understood. If we assume that the evaporating atoms can be characterized by a Maxwellian-Boltzmann velocity distribution in the vapor,[3] the shape of the pulse of atoms arriving at the needle is given by the convolution integral over all arrival times of the heat pulse at the surface with the Maxwellian-Boltzmann distribution. This pulse shape might be modified considerably by the phonon-evaporating atom process.

Assuming, however, that the surface conversion process does not change the pulse shape, then by looking at the start of the heat-pulse curve at the detector, we can make

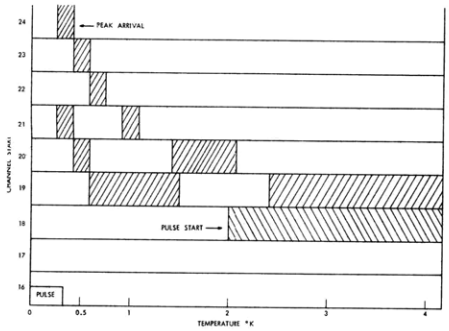

Fig. I-17.

Calculated arrival times for 50-μs square pulse as a function of gas temperature.

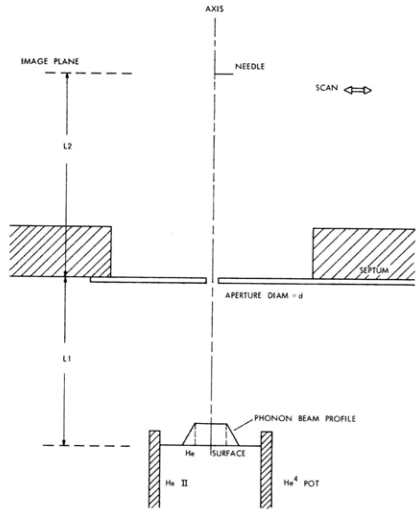

Fig. I-18.

Scanning molecular microscope mode magnification M = L2/L1. Diameter of resolution r = d(1+L1/L2).

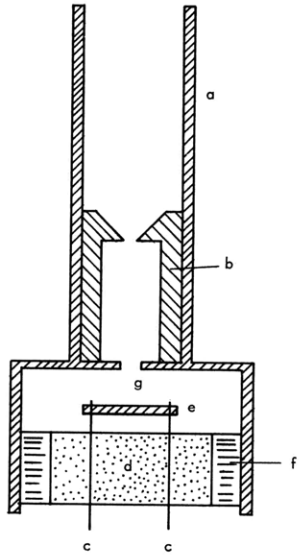

(a) POT
(b) COLLIMATING INSERT
(c) COPPER WIRE LEAD TO HEATER
(d) EPOXY CORE
(e) HEATER
(f) HEATER INSERT
(g) COLLIMATING APERTURE

Fig. I-19.

He^4 pot for collimated phonon beam.

some estimates of the effective temperature of the evaporating atoms.

A program has been written that convolves a square pulse with the Maxwellian-Boltzmann distribution at various gas temperatures, and plots the intensity at the detector as a function of the time of arrival. In Fig. I-17 we plot the start of the convolved pulse and the peak as a function of temperature for a 50-μs pulse starting in channel 16. We see that above 2°K the arrival times do not change very much with temperature but are all grouped in channel 18. Below this temperature the arrival times are increasingly delayed as the temperature is decreased. Comparing this model with experiment in Fig. I-16, we see that the temperature of the evaporated atoms varies considerably as the energy/pulse changes.

Two assumptions contained in this model are open to question. First is the assumption that the frequency response of the surface is good, in that a square pulse of phonons incident on the surface gives a square pulse of evaporating atoms. The second assumption is that the start of the experimental curve is attributable to atoms that were evaporated while the square pulse of phonons arrived at the surface. In the actual experiment, the pulse of phonons arriving at the surface is only square at the start of the pulse and then changes shape, because of the diffusive arrival of phonons from the heat pulse.

If we could separate those phonons arriving at the surface without collisions with the walls of the container from those that make up the diffusive pulse (i.e., make a collimated phonon beam), we might be able to get a clearer picture of the processes involved in the conversion of phonons into evaporating atoms.

If the evaporation arising from the collimated phonon beam is restricted to the area of the phonon-beam profile, then by using the needle as a molecular microscope[4] (Fig. I-18) we should be able to see this localized evaporation. For this purpose we have designed and built a new He^4 pot (Fig. I-19). With this pot we shall have a collimated phonon beam of 0.0225 in. diameter and edge spread that varies depending on the amount of collimation and surface-heater depth. Tests are now being carried out with this new configuration.

W. B. Davis

References

1. W. B. Davis, Quarterly Progress Report No. 102, Research Laboratory of Electronics, M.I.T., July 15, 1970, pp. 1-6.
2. H. C. Kramers et al., Physica 20, 743 (1954).
3. J. W. McWane, Ph.D. Thesis, Department of Physics, M.I.T., 1970 (unpublished).
4. J. C. Weaver and J. G. King, Quarterly Progress Report No. 98, Research Laboratory of Electronics, M.I.T., July 15, 1970, pp. 9-12.

E. DETECTION OF A QUANTIZED VORTEX LINE AT A KNOWN LOCATION

One of the fundamental problems in superfluid helium research concerns the existence and properties of quantized vortex lines. Several experiments have already provided impressive evidence for their existence under certain conditions.[1-3] No experiment, however, has succeeded in detecting the appearance of a vortex at a known location. We report here a summary of progress with an experiment designed to detect the appearance of a vortex line at a well-defined pinning site.

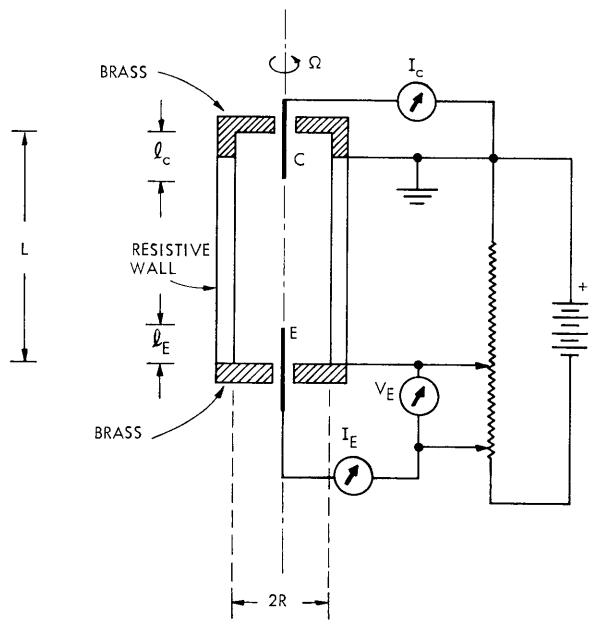

Fig. I-20. Schematic diagram of the apparatus.

A schematic version of the apparatus is shown in Fig. I-20. A pair of needles (E = emitter, C = collector) of shank radii a_1 are positioned on axis within a cylindrical cavity of radius R, so that the currents I_E and I_C can be monitored. The tip of E is etched to a sharp point (radius of curvature ~10^3 Å) so that suitable field emission of electrons occurs for V_E of 200-400 volts. The cylindrical cavity is filled with liquid helium, and can be rotated at angular velocity Ω with respect to the axis.

In essence the experiment studies the collected current, I_C, as a function of Ω for a constant emitted current, I_E. For each run the apparatus is first cooled slowly to below T_λ, I_E and I_C are measured, and then the apparatus is gently accelerated. At a critical angular velocity, Ω_{C1}, it is energetically favorable for a macroscopic quantum transition

to occur from no quantized vortex line (n = 0) to a single quantized vortex line (n = 1) pinned between E and C. The electrical conducting properties of the system should be detectably different for the n = 0 and n = 1 states, and should allow detection of the transition if we monitor I_C as Ω is varied. Furthermore, after some value of Ω_{max} is reached the system is slowly decelerated and returned to rest, after which I_E and I_C are again measured. In addition to seeking a transition during acceleration, comparison of (I_C/I_E) before and after rotation should also reveal the presence of a vortex line at the pinning site.

The theoretical value of Ω_{C1} is obtained by considering the rotational free energy, F, of the system. If the needles C and E were absent, the transition would be expected to occur at $\Omega = \Omega^o_{C1}$, given by the well-known expression

$$\Omega^o_{C1} = \frac{k}{2\pi R^2} \ln\left(\frac{R}{a_o}\right); \qquad k = \frac{h}{m}, \tag{1}$$

where h is Planck's constant, m is the mass of a helium atom, and a_o is the vortex core radius. In our case we obtain

$$\Omega_{C1} \approx \Omega^o_{C1} - \frac{k}{2\pi R^2}\left(\frac{\ell_C + \ell_E}{L}\right) \ln\left(\frac{a_1}{a_o}\right) \tag{2}$$

for the angular velocity at which free-energy considerations favor a state with n = 1 quantized circulation around the needles and which blends smoothly into a vortex line of n = 1 between the needle tips. Numerically, $\Omega^o_{C1} = 1.8 \times 10^{-1}$ rad-sec^{-1}, whereas $\Omega_{C1} = 0.8 \times 10^{-1}$.

It may also be possible to create vortex-line states with n > 1 in our type of apparatus, in particular n = 2. This possibility arises because the usually prohibitive higher free energy of a length of an n = 2 vortex line can be compensated by a long section of n = 2 quantized circulation about the relatively thick needle shanks where the free energy is relatively low. A vortex line with n > 1 has never been observed and would be of considerable interest.

Electrons emitted by E exist in liquid helium as bubbles with a radius of ~15 Å, a phenomenon that is due primarily to the balancing of the quantum-mechanical zero-point pressure of the electron against the ambient pressure of the liquid helium. The bubble model provides an explanation for the electron's mobility in liquid helium and also explains the trapping of electrons on a vortex line.[4] In the absence of a vortex line between E and C, electrons emitted from E which are mobility-dominated follow the electric field lines within the apparatus. If C is well shielded so that essentially no field lines originate from C, then $I_C = 0$ in the absence of a vortex. If C is unshielded, however, some field lines originate at C and the ratio (I_C/I_E) is small, but not zero in the

absence of a vortex. A computer calculation of the field lines yields the estimate $(I_C/I_E) \approx 10^{-2}$ in the absence of a vortex, a value that is in rough agreement with preliminary data.

On the other hand, if a vortex line is present between E and C, and C is well shielded, then some electrons are trapped on the vortex and are channeled to C. Under reasonable operating conditions, the channeled electron current should be of the order of $I_C \approx 5 \times 10^{-16}$ A. If C is unshielded, however, and a vortex is present, then I_C should be less than that obtained without a vortex. The decrease in I_C in the unshielded case arises from two possible effects: (i) a deflection of otherwise collected electrons away from C, because of trapped charge on the vortex line, and (ii) a decrease in effective conductivity between E and C, because of the partial masking of E by the vortex. The second effect results from the higher electron mobility in bulk liquid helium (μ_B) compared with the mobility along a vortex (μ_V). It appears that when the needle is unshielded the effect is larger, and this case is now being studied. Thus far, no reliable transitions have been observed during rotation, but for runs in which the maximum angular velocity exceeded Ω_{C1} the following transitions were often observed.

$(I_C/I_E) \approx 10^{-2}$ (before rotation)

$(I_C/I_E) \approx 10^{-4}$ (after rotation).

Subsequent warming to above T_λ restores the "before rotation" value, and strongly suggests that the transition to a vortex line pinned between E and C has occurred.

We are grateful for stimulating conversations with J. G. King and are indebted to M. G. R. Thomson for help with the computer calculations.

S. R. Jost, J. C. Weaver

References

1. W. F. Vinen, Proc. Roy. Soc. (London) A260, 218 (1961); see also S. C. Whitmore and W. Zimmermann, Jr., Phys. Rev. 166, 181 (1967).
2. G. W. Rayfield and F. Reif, Phys. Rev. Letters 11, 305 (1963).
3. R. E. Packard and T. M. Sanders, Jr., Phys. Rev. Letters 22, 823 (1969).
4. R. J. Donnelly, Experimental Superfluidity (University of Chicago Press, Chicago, Ill., 1967), Chap. 6.

F. SCANNING WATER MOLECULAR MICROSCOPE

During the past several years a molecular microscope has been developed for making visible pictures of the spatial variation in the emission from a sample[1,2] of neutral

volatile molecules (such as water). A sketch of the current version is shown in Fig. I-21. It incorporates a scanning pinhole rather than a scanning detector.

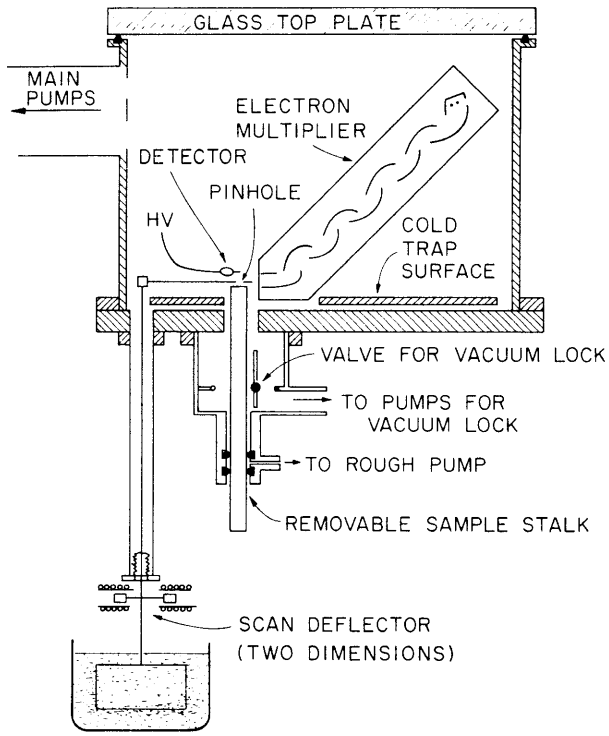

Fig. I-21. Schematic diagram of the apparatus.

A conventional pinhole microscope is shown in Fig. I-22a, and Fig. I-22b shows the location of the field ionization detector and electron multiplier in the present

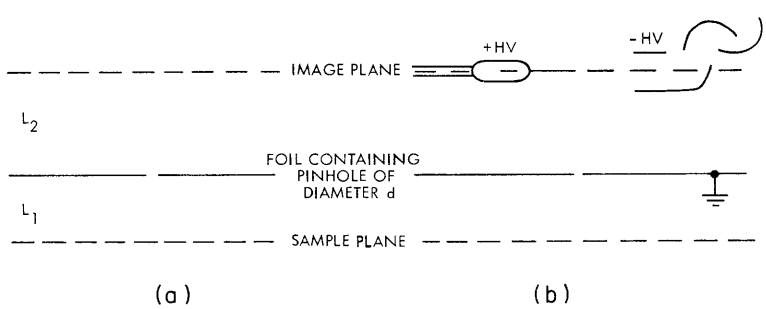

Fig. I-22. (a) Idealized version.
(b) Present device.

device. Ordinarily the pinhole (diameter, d) is stationary and emissions from the sample are imaged at the image plane with magnification, M, given by

$$M = L_2/L_1 \tag{1}$$

and a geometrically limited resolution, r, given by

$$r = d\left(1 + \frac{L_1}{L_2}\right). \tag{2}$$

For the pinhole we are now using ($d = 1.2 \times 10^{-2}$ cm), the diffraction of water molecules because of their de Broglie wavelength (10^{-8} cm) is negligible.

If neutral molecules are converted directly into a visible image over the entire image plane by chemical and physical means (for example, by providing a cold metal surface at the image plane, capturing a latent image of molecules there, and subsequently developing the latent image into a visible image – which has not yet been satisfactorily accomplished), then Eqs. 1 and 2 for the magnification and resolution are applicable. These equations also apply if a small-area detector (such as a field ionization detector; $A_{det} \approx 10^{-11}$ cm^2) can be scanned successfully in the image plane to pointwise-sample the flux of neutral molecules into the image plane.

Experience, however, shows that this method does not work satisfactorily with a field-ionization detector. Instead, spurious but reproducible pictures are obtained that are independent of a water-emitting sample. Because the operation of the field-ionization detector is not completely understood, the reason for the failure of this method is not completely understood. It is clear, however, that electric field lines must change within the apparatus when the field-ionization detector is scanned, since there are high potentials on the detector (+5-+10 kV) and on the multiplier (-3 kV) with respect to the irregularly shaped (but grounded) walls of the apparatus. Because of the high potentials of the detector and multiplier with respect to the grounded walls of the apparatus, scanning the field-ionization detector results in changing electric field lines. As a result, the collection efficiency of the multiplier, the ionization of background gas at 10^{-7} Torr, and so forth, can all vary during scanning.

To overcome this problem, we placed a grounded scanning foil with pinhole ($d \approx 1.3 \times 10^{-2}$ cm) behind a large grounded mask that contained a relatively large ($d = 3 \times 10^{-1}$ cm) hole. The entire scan occurs within the large hole. The combination of scanning foil and mask allows scanning without appreciably changing electric field

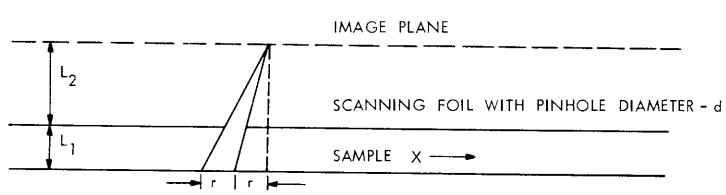

Fig. I-23. Sketch for calculating magnification.

lines, and successful operation is achieved. While the resolution is still given by (1) for a scanning pinhole, inspection of Fig. I-23 shows that the magnification, M, is now

$$M = \left(\frac{X_{dis}}{X_{scan}}\right)\left(\frac{X_{scan}}{X_{sample}}\right) = \left(\frac{X_{dis}}{X_{scan}}\right)\frac{d}{r} = \left(\frac{X_{dis}}{X_{scan}}\right)\frac{L_2}{L_1 + L_2}, \tag{3}$$

where X_{dis} is the peak-to-peak length of the scan as displayed on the final photograph, X_{scan} is the peak-to-peak distance traversed by the pinhole during the scan, and X_{sample} is the actual peak-to-peak length exposed to the detector during the scan. For the present scanning molecular microscpoe

$$d = 1.3 \times 10^{-2} \text{ cm}$$

$$L_1 = 5 \times 10^{-1} \text{ cm}$$

$$L_2 = 1 \text{ cm},$$

so that $r = 2 \times 10^{-2}$ cm and $M = (6.7 \times 10^{-1})(X_{dis}/X_{scan})$. As shown in three typical pictures (Figs. I-26 through I-28), this scanning molecular microscope has a useful resolution and magnification, and has the potential to provide information unobtainable by either optical or electron (ion) microscopy.

For Figs. I-26 through I-28 the resolution is always 2×10^{-2} cm, while the magnification varies as indicated. Figure I-26 shows water evaporating from 4 to 24 holes in a plexiglas sheet, with diam 2×10^{-2} cm and length 1.5×10^{-1} cm. As shown in Fig. I-24, a plexiglas sheet overlays a buffer material that has a moderate permeability,

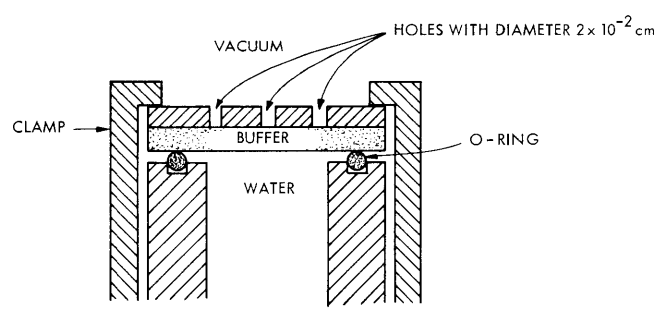

Fig. I-24. Test pattern for sample configuration.

with liquid water available on the underside of the buffer. This sample was intended primarily as a known test pattern, and has no other significance.

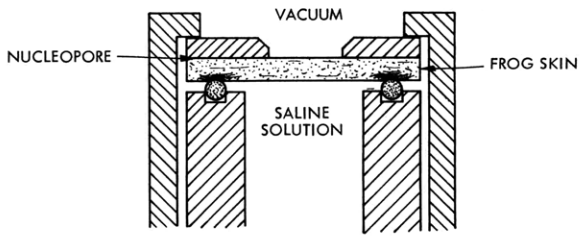

Fig. I-25. Sample holder containing frog skin.

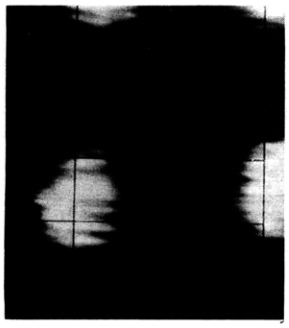

Fig. I-26. Test pattern.

Fig. I-27. Frog skin.

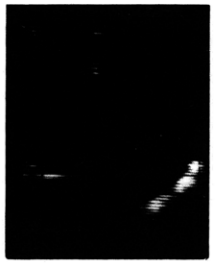

Fig. I-28. Tooth sample.

The picture in Fig. I-27 was obtained from the sample shown schematically in Fig. I-25. As shown, the sample is a frog skin (Rana pipiens) with an overlay on a single sheet of 1-μ pore size, 10-μ thick, nucleopore filter paper which provides a porous supporting sheet with a high density of pores well below our resolution. Over this is a plexiglas sheet with a 1.5×10^{-1} cm hole. The underside of the frog skin is bathed in an appropriate saline solution. As might be expected, water crossing the frog skin within the hole can evaporate directly into the vacuum, while water crossing in regions masked by the opaque (to water) plexiglas can migrate laterally until it reaches the edge of the hole, where it evaporates. Thus a ring of evaporating water should be observed (although the ring need not be uniform in its evaporation if the regions of frog skin which supply it have varying properties). The picture shows a portion of this nonuniform ring plus a region of higher water flux inside the ring. This region of higher water flux reveals a feature of the frog skin which is not apparent optically and, although we do not yet know the cause of this feature (perhaps it is a region of tissue damage), the ability to detect an otherwise invisible region with higher water permeability is significant.

Figure I-28 shows varying water emission from the edges of an irregular sample of a tooth mounted in a piece of plexiglas.[3] Water is present on the nonvacuum side. Dental researchers are keenly interested in the porosity of teeth and tooth samples to

water, but this porosity, which can evidently vary spatially within an individual tooth, cannot be satisfactorily measured by existing techniques. Some of the nonuniform water emission shown in Fig. I-28 is apparently the result of water following the paths of least resistance through portions of the tooth sample where it is nonuniformly sealed into the plexiglas piece. This information cannot be provided by optical or electron microscopy. In this case the magnification is approximately 10X.

J. C. Weaver, J. G. King

References

1. J. C. Weaver and J. G. King, Quarterly Progress Report No. 98, Research Laboratory of Electronics, M.I.T., July 15, 1970, pp. 9-12.
2. J. G. King and J. C. Weaver, "Molecular Microscopy," to be published in H. E. Stanley (Ed.), Biomedical Physics and Biomaterials Science.
3. This sample was kindly provided by Dr. D. Williams and Dr. R. Manley of the Tufts Dental School.

G. DESORPTION HEAT PULSE PROPAGATION

It is probable that an important version of the molecular microscope will use a scanning electron beam to desorb previously applied neutral molecular stains (NMS).[1] In such a device it is envisioned that a biological specimen (such as a cell membrane surface) will be initially stained by exposure to a flux of an appropriate neutral molecule such as water. In this example, water should specifically bind to hydrophilic regions of the surface, and subsequent desorption of water molecules by the focused beam of electrons can map out the location of the hydrophilic sites. As a preliminary study we examine the heat propagation from an electron beam pulse that delivers heat to a thin disk in a substrate with thermal conductivity K, density ρ, specific heat C (representing the thermal properties of a biological specimen).

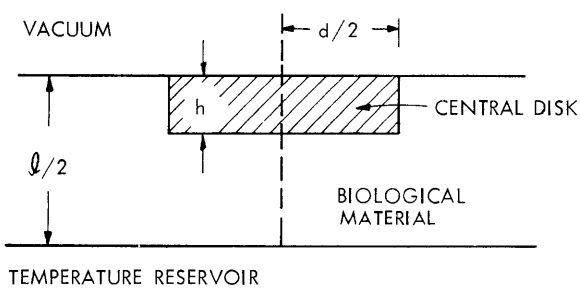

Fig. I-29.
Physical geometry for calculation of heat propagation.

We first examine the approximate time constants for loss of heat from the substrate, because of conduction and radiation, and find that conduction dominates. The physical geometry is shown in Fig. I-29. If T is the temperature, then the radiation time constant τ_R for the disk, given an initial heat input Q, is approximately

$$\tau_R \approx \frac{Q}{\dot{Q}_R} = \frac{Ch\rho}{\epsilon\sigma\,(T+T_o)\left(T^2+T_o^2\right)} . \tag{1}$$

We expect $T \gg T_o$, so that $\tau_R \approx (Ch\rho)/(\epsilon\sigma T^3)$. Similarly, the conduction time constant is

$$\tau_K \approx \frac{Q}{\dot{Q}_K} = \frac{Cr_o h^2 \rho}{K(r_o+2h)} , \tag{2}$$

since $h \approx r_o = d/2$. Thus $\tau_K \approx (Ch^2\rho)/3K$, and the relative values become $\gamma = \frac{\tau_R}{\tau_K} = \frac{3K}{\epsilon\sigma T^3 h}$. If $T \approx 250°K$, $\epsilon \sim 1$, $\sigma = 6 \times 10^{-5}$ erg-sec^{-1}-cm^{-2}-°K^{-1}; $h = 1 \times 10^{-6}$ cm, and the conductivity for polyethylene at 80°K is $K = 2 \times 10^3$ erg-sec^{-1}-cm^{-2}-°K^{-1}, then $\gamma \approx 6 \times 10^6$, so that the heat loss by conduction is vastly greater than that by radiation.

To study the propagation of heat delivered instantaneously into a thin disk (diameter d, thickness h), we take the ideal case of an infinite slab in the x-y plane of finite thickness $\ell/2$ in the z direction. The z = 0 surface is held at a constant temperature (for convenience, we pick T = 0; we can subsequently add a constant temperature to the solution). Since we have shown that the radiative heat loss is negligible, we consider the more easily solved symmetric case given below, with twice the heat input, since by symmetry no heat will flow across the $z = \ell/2$ plane.

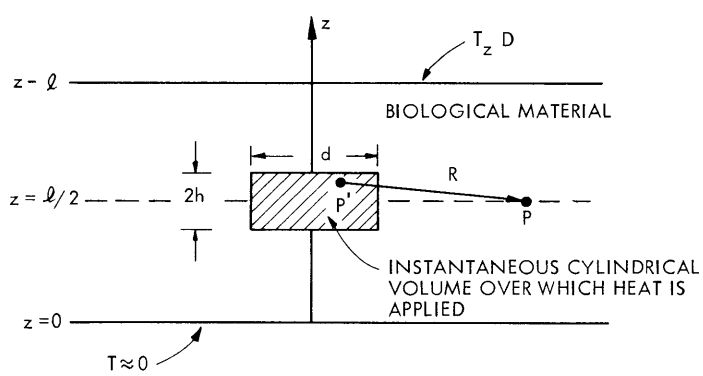

Fig. I-30. Modified mathematical geometry for calculation of heat propagation.

We thus consider the geometry shown in Fig. I-30. The temperature per unit volume at point $P(x, y, \ell/2, t)$, because of an instantaneous point source P' at (x', y', z', t') in this configuration is a Green's function,[2] T_G, given by

$$T_G(R;\, t-t') = \frac{Q}{\pi\rho c\kappa\ell}\,\frac{\exp[-R^2/4\kappa(t-t')]}{(t-t')}\sum_{n=1}^{\infty}\exp[-b_n(t-t')]\,\sin\frac{n\pi z'}{\ell}\,\sin\frac{n\pi}{2}, \tag{3}$$

where

κ = diffusivity = $K/\rho c$

$$R^2 = (x-x')^2 + (y-y')^2 = r^2 + r'^2 - 2rr'\cos\theta'$$

$$b_n = \left(\frac{\pi^2\kappa}{\ell^2}\right)h^2.$$

The coordinates are clarified in Fig. I-31. To find the physical temperature, within

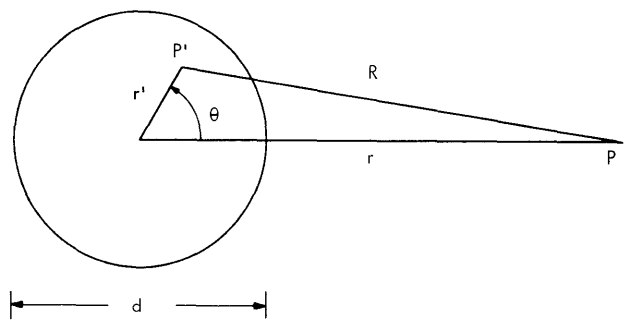

Fig. I-31. Coordinates for calculation of heat propagation.

the $z = \ell/2$ plane, $T(r, t-t')$, from an instantaneous source at t', we need to integrate T_G over the volume of the source. Thus

$$T = \left[\frac{Q}{\pi\rho C\kappa\ell}\right]\frac{1}{(t-t')}\int_0^{2\pi} d\theta' \int_0^{d/2} \exp[-(r^2+r'^2-2rr'\cos\theta')/4\kappa(t-t')]\, r'\, dr'$$

$$\int_{(\ell/2)-h}^{(\ell/2)+h} dz' \sum_{n=1}^{\infty}\exp[-b_n(t-t')]\,\sin\frac{n\pi}{2}\,\sin\frac{n\pi z'}{2}. \tag{4}$$

We integrate first with respect to z' and obtain

$$\int_{(\ell/2)-h}^{(\ell/2)+h} dz'\,\sin\frac{n\pi z'}{\ell} = \frac{2\ell}{h\pi}\,\sin\frac{n\pi}{2}\,\sin\left(\frac{n\pi h}{\ell}\right). \tag{5}$$

Then the sum over n becomes

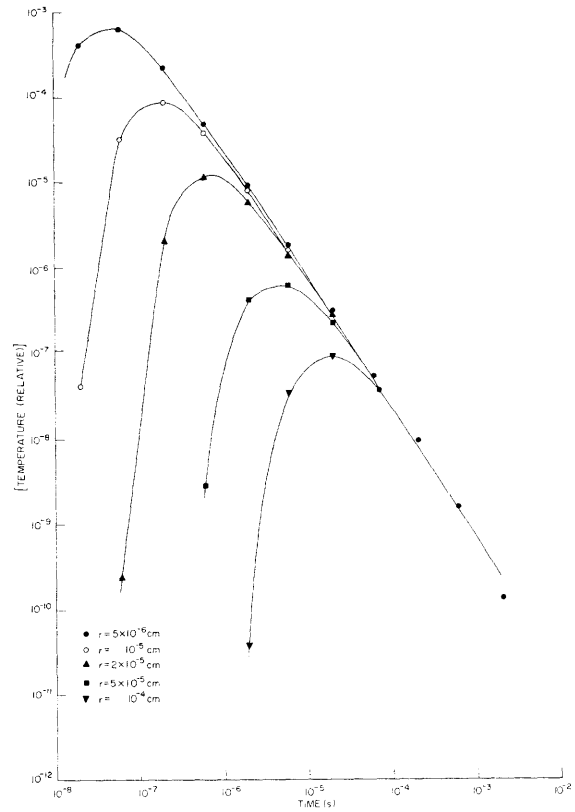

Fig. I-32. Temperature rise (arbitrary units) as a function of time for various values of r. Heating pulses on for the first 10^{-6} s.

Table I-1. Ratio of peak temperature rise at $z = \ell/2$ as a function of r when $r = 5 \times 10^2$ Å is taken for a reference. The approximate time of occurrence of $T_{peak}(r)$ after application of the instantaneous source of heat is also given.

r (angstroms)	$\frac{T_{peak}(r)}{T_{peak}(500\ \text{Å})}$	t_{peak} (seconds)
5×10^2	1.0	4×10^{-8}
1×10^3	1.3×10^{-1}	2×10^{-7}
2×10^3	1.5×10^{-2}	6×10^{-7}
5×10^3	9.2×10^{-4}	6×10^{-6}
1×10^4	1.3×10^{-4}	2×10^{-5}

$$\sum_{n=1}^{\infty} \exp[-b_n(t-t')] \left(\frac{2\ell}{n\pi}\right) \sin^2\left(\frac{n\pi}{2}\right) \sin\left(\frac{n\pi h}{\ell}\right) = \frac{2\ell}{\pi} \sum_{\substack{n=1 \\ n \text{ odd}}}^{\infty} \frac{\exp[-b_n(t-t')]}{n} \sin\frac{n\pi h}{\ell}. \tag{6}$$

We now integrate with respect to θ', using the relation[3]

$$\int_0^{\pi} e^{-i\beta \cos x} \cos \nu x \, dx = i^{\nu} \pi J_{\nu}(\beta), \tag{7}$$

with $\nu = 0$. By using the series representation[4]

$$J_{\nu}(x) = \left(\frac{x}{2}\right)^{\nu} \sum_{j=0}^{\infty} \frac{(-1)^j \left(\frac{x}{2}\right)^{2j}}{j!\, \Gamma(j+\nu+1)}, \tag{8}$$

the integration over the spot radius, r', can be performed, since[5]

$$\int x^j e^{ax} dx = e^{ax} \sum_{m=0}^{m=j} \frac{(-1)^m j!\, x^{j-m}}{(j-m)!\, a^{m+1}}; \quad a = -1. \tag{9}$$

Our final expression for the temperature rise for an instantaneous disk source is thus

$$T(r,p) = \left[\frac{16Q}{\pi\rho C}\right] \left\{1 - \exp\left[-p\left(r^2 + \frac{d^2}{4}\right)\right] \sum_{j=0}^{\infty} \frac{(pr^2)^j}{j!} \sum_{m=0}^{m=j} \frac{(pd^2/4)^{j-m}}{(j-m)!}\right\}$$
$$\sum_{\substack{n=1 \\ n \text{ odd}}}^{\infty} \frac{\exp\left[-\frac{b_n}{4\kappa p}\right]}{n} \sin\frac{n\pi h}{\ell}, \tag{10}$$

where $p = [4\kappa(t-t')]^{-1}$ Equation 10 has been evaluated numerically as $T(t)$ by setting $t' = 0$, $\ell = 10^{-3}$ cm, $h = 10^{-6}$ cm, $d = 10^{-6}$ cm for several values of r. These results are plotted in Fig. I-32. As expected, the peak temperature rise falls off rapidly with increasing r, a necessary feature if the scanning desorption molecular microscope is to be feasible. Table I-1 shows the relative peak temperature rise and the approximate time at which it occurs.

This investigation continues and will include the effect of finite heat pulsewidth. Our final aim is to estimate the number of water molecules desorbed per area as a function of r for various conditions. We acknowledge helpful conversations with J. G. King and G. R. Herzlinger and wish to thank M. G. R. Thomson for carrying out all the numerical calculations.

D. G. Payan, J. C. Weaver

References

1. J. G. King and J. C. Weaver, "Molecular Microscopy," to be published in H. E. Stanley (Ed.), Biomedical Physics and Biomaterials Science.
2. H. S. Carslaw and J. C. Jaeger, Conduction of Heat in Solids (Oxford University Press, London, 2d ed., 1959), Equation (12), pp. 372-378.
3. J. S. Gradshteyn and J. M. Ryzhik, Tables of Integrals Series and Products (Academic Press, Inc., New York, 4th ed., 1965), Equation 5.915-2, p. 482.
4. Ibid., Equation 8.440, p. 959.
5. Ibid., Equation 2.321-2, p. 92.

H. NEW METHOD FOR STUDYING WATER TRANSPORT IN BIOLOGICAL MEMBRANES

The transport of molecules and ions across biological membranes has received considerable attention for several decades but understanding of the fundamental mechanisms of transport, for the most part, is still lacking.[1] One class of problems of particular interest concerns the change in permeability to water membranes following the application of certain drugs. A specific example is the increase in water permeability of frog skin following the application of ADH (antidiuretic hormone). This effect is usually measured by mounting a freshly obtained sample of frog skin (area ≈ 7 cm^2) in a plastic chamber so that both sides of the skin can be bathed with an appropriate oxygenated saline solution (Ringer's solution). The conventional method for measuring the water flux in such an apparatus involves a volumetric technique in which the change in volume of water on one side of the frog skin is measured at regular time intervals ($\sim$10 min). This method yields a time-integrated value of the water flux over 10 min, so that the temporal resolution is poor. The conventional method is also somewhat insensitive, with a minimum detectable flux of the order of 0.2 $\mu\ell$/min-cm^2, or $\sim 10^{17}$ molecules/sec-cm^2.

We report here our progress in the development of a new technique for studying water transport in samples of surviving frog skin. This technique, which is essentially a special case of molecular microscopy without spatial resolution, offers the possibility of increasing the sensitivity by several orders of magnitude, as well as considerably improving the time response. Our technique involves placing the frog skin in an environment where it is fully bathed with circulating aerated Ringer's solution on one side while the other side is a vacuum (with an intermediary of buffering nucleopore filter paper). This arrangement is shown in Fig. I-33. On the vacuum side a field ionization detector and electron multiplier monitor the flux of water into the vacuum by counting individual water molecules. In the present apparatus it is feasible to expect detection of a water flux of 10^{13} molecules/sec-cm^2. If an electron bombardment universal

ionizer[2, 3] and mass spectrometer are employed instead, we can hope to monitor a flux at the 5×10^{10} molecules/sec-cm^2 level. In both cases the intrinsic time response of the apparatus is determined by the sample-detector separation and thermal velocities, and is of the order of 10^{-4} s.

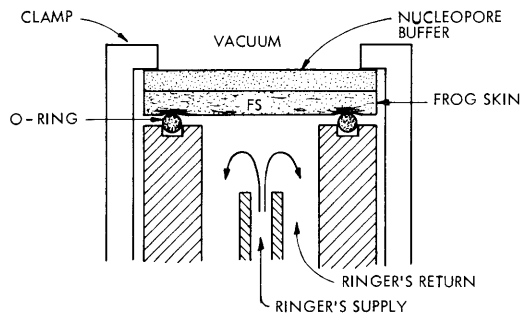

Fig. I-33.
Sample of configuration.

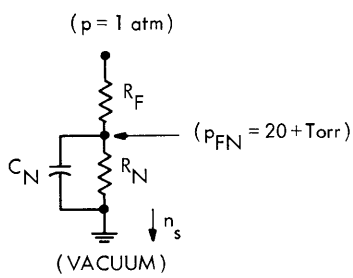

Fig. I-34.
Equivalent circuit for water movement. P is analogous to voltage; $\dot{n}_s$ (molecules-sec^{-1}) is analogous to current. R_F is the passive resistance of frog skin to water, R_N is the resistance of nucleopore filter paper, and C_N is the capacitance associated with the porous nucleopore.

Clearly, a formidable problem is the maintenance of a viable frog-skin sample, since the sample may undergo stress from an atmospheric pressure differential, as well as the dehydrating effects of vacuum on one side. Experiments on the frog-skin sample with both sides bathed in Ringer's solution while a 1-atm pressure differential was maintained showed no damaging effects, however. As in all of our determinations, the open-circuit potential developed by the frog skin is used as the indicator of viability. Similar experiments with both sides at 1 atm but with one side dried by a gentle stream of air indicated that dehydration would easily kill the sample. Thus the following approach was tried, as shown schematically in Fig. I-34. The purpose of our approach is to provide sufficient resistance to water flow between the frog-skin sample and the vacuum so as to achieve a partial pressure of water at the frog skin-nucleopore interface, P_{FN}, equal to or somewhat greater than 20 Torr, the vapor pressure of water at room temperature. In this way the otherwise severe dehydration effects can be avoided while still allowing a direct and sensitive measure of the water flux by our detector, since one or more monoplayers of water should be able to exist on the side of the frog skin toward vacuum. We have performed some tests in a small test system using this approach, and find that in many, but not all, instances the frog skin survives exposure

to vacuum for 1 hour. This is an encouraging but preliminary result, and our tests will continue.

One disadvantage of our approach is some sacrifice in temporal resolution over the intrinsic resolution ($\sim 10^{-4}$ s) of the apparatus. The cause is as follows: In addition to the resistance of the nucleopore, R_N, there is also a non-negligible capacitance, C_N, because of the usual capacitance of a void volume for a gas ($C_{NV} = n/p$), and also because of an adsorption isotherm for water and the nucleopore ($C_{NA} = \partial n/\partial p$). Thus $C_N = C_{NV} + C_{NA}$ and gives rise to a calculated time constant of the order of 1 s or less. Measured time constants are in rough agreement at 1-3 s. Nevertheless, the temporal resolution is much better than that obtained in the traditional volumetric method.

Since our technique is still somewhat unreliable, only a few runs have been made in the main apparatus in which the water flux can be measured. With normal dosages of ADH, no noticeable flux change has been observed. In a single run for which the ADH dose was excessively large, however, the response sketched in Fig. I-35 was seen.

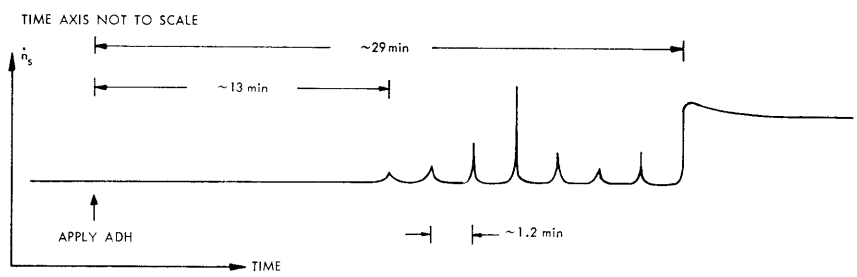

Fig. I-35. Water flux as a function of time following a massive dose of ADH.

This behavior is quite usual. It should be emphasized that the spikes would not have been seen in conventional measurements. Because this behavior has been observed only once, we attribute no fundamental significance to it except as a demonstration of the type of signal that can easily be observed by our technique.

Finally, although it might at first glance appear far-fetched, we wish to point out that this in vitro technique can probably be extended to in vivo applications, at least in the case of frog skin, by placing a live frog up to a vacuum port (again using a suitable buffer). Naturally the entire technique described here can be readily extended to study transport of gases such as O_2 and CO_2. During the recent development of this technique we have had considerable help from many members of our group, especially J. Jarrell, and also from Dr. A. Essig of the New England Medical Center.

J. C. Weaver, J. Abrams, J. G. King

[J. Abrams is a visiting student from the Department of Biochemistry, Harvard University.]

References

1. H. H. Ussing, "Active Transport," in Theoretical Physics and Biology, Proc. First International Conference on Theoretical Physics and Biology (Interscience Publishers, Inc., New York, 1969), p. 179.

2. R. Whittam and K. P. Wheeler, "Transport across Cell Membranes," Ann. Rev. Physiol. 32, 21-57 (1970).